

Star formation in $z > 1$ 3CR host galaxies as seen by *Herschel**

P. Podigachoski¹, P. D. Barthel¹, M. Haas², C. Leipski³, B. Wilkes⁴, J. Kuraszkiewicz⁴, C. Westhues², S. P. Willner⁴,
M. L. N. Ashby⁴, R. Chini², D. L. Clements⁵, G. G. Fazio⁴, A. Labiano⁶, C. Lawrence⁷, K. Meisenheimer³,
R. F. Peletier¹, R. Siebenmorgen⁸, and G. Verdoes Kleijn¹

¹ Kapteyn Astronomical Institute, University of Groningen, 9747 AD Groningen, The Netherlands
e-mail: podigachoski@astro.rug.nl

² Astronomisches Institut, Ruhr Universität, D-44801 Bochum, Germany

³ Max-Planck Institut für Astronomie (MPIA), D-69117 Heidelberg, Germany

⁴ Harvard-Smithsonian Center for Astrophysics, Cambridge, MA 02138, USA

⁵ Astrophysics Group, Imperial College London, Blackett Laboratory, Prince Consort Road, London SW7 2AZ, UK

⁶ Institute for Astronomy, Department of Physics, ETH Zurich, Wolfgang-Pauli-Strasse 27, CH-8093 Zurich, Switzerland

⁷ Jet Propulsion Laboratory, California Institute of Technology, 4800 Oak Grove Drive, Pasadena CA 91109, USA

⁸ European Southern Observatory, Karl-Schwarzschild-Str. 2, 85748 Garching b. München, Germany

Received ; accepted

ABSTRACT

We present *Herschel* (PACS and SPIRE) far-infrared (FIR) photometry of a complete sample of $z > 1$ 3CR sources, from the *Herschel* GT project *The Herschel Legacy of distant radio-loud AGN* (PI: Barthel). Combining these with existing *Spitzer* photometric data, we perform an infrared (IR) spectral energy distribution (SED) analysis of these landmark objects in extragalactic research to study the star formation in the hosts of some of the brightest active galactic nuclei (AGN) known at any epoch. Accounting for the contribution from an AGN-powered warm dust component to the IR SED, about 40% of our objects undergo episodes of prodigious, ULIRG-strength star formation, with rates of hundreds of solar masses per year, coeval with the growth of the central supermassive black hole. Median SEDs imply that the quasar and radio galaxy hosts have similar FIR properties, in agreement with the orientation-based unification for radio-loud AGN. The star-forming properties of the AGN hosts are similar to those of the general population of equally massive non-AGN galaxies at comparable redshifts, thus there is no strong evidence of universal quenching of star formation (negative feedback) within this sample. Massive galaxies at high redshift may be forming stars prodigiously, regardless of whether their supermassive black holes are accreting or not.

Key words. galaxies: active – galaxies: high-redshift – galaxies: star formation – infrared: galaxies

1. Introduction

The understanding that most (if not all) galaxies in the Universe host a supermassive black hole (SMBH) is among the most important findings of modern astronomy. The growth of a SMBH through mass accretion generates large amounts of energy during a phase in the evolution of the galaxy known as an active galactic nucleus (AGN) phase. Although there is a difference of a factor of $\sim 10^9$ in their physical size scales, the SMBHs and their host galaxies exhibit strong scaling relations (e.g. Magorrian et al. 1998; Tremaine et al. 2002; Gültekin et al. 2009), suggesting a link between the growth of the SMBHs and that of their host galaxies. Moreover, both these processes are thought to peak at redshifts $z \sim 2$ (e.g. Hopkins & Beacom 2006; Alexander et al. 2008). The symbiosis of black hole and global galaxy growth is intriguing because of the possible feedback effects: positive (AGN inducing star formation) and/or negative (AGN quenching of star formation). These feedback processes are of paramount importance for our understanding of galaxy formation (e.g. Croton et al. 2006; Hopkins et al. 2008). However, neither the feedback mechanisms nor the overall impact of feedback on the host galaxies is known. Other big unknowns are

the duration and frequency of AGN accretion and host galaxy star formation phases.

High redshift radio-loud AGN ($P_{1.4 \text{ GHz}} > 10^{25} \text{ W Hz}^{-1}$ and $z > 1$) provide a unique opportunity to probe the interplay between the growth of the black hole and the hosting stellar bulge. They are invariably associated with massive galaxies having $M_{\text{stellar}} \gtrsim 10^{11} M_{\odot}$ (Best et al. 1998; Seymour et al. 2007; De Breuck et al. 2010), and have edge-brightened, double-lobed, FRII morphologies (Fanaroff & Riley 1974) that permit estimates of the duration of the episode of strong AGN activity. In addition to being used in studies of massive galaxy evolution, radio-loud AGN are being used extensively in unification studies, where, distant radio-loud galaxies and quasars are believed to make up one and the same population (Barthel 1989; Antonucci 1993; Urry & Padovani 1995), hence have equally massive hosts. Ultraviolet or visible opaque circumnuclear dust is an essential element of this scenario; distant 3CR quasars and radio galaxies are indeed luminous mid-infrared (MIR) emitters (Siebenmorgen et al. 2004; Haas et al. 2008; Leipski et al. 2010).

It has long been suspected that hosts of powerful high-redshift radio-loud AGN undergo episodes of vigorous (dust obscured) star formation (e.g. Archibald et al. 2001). Huge reservoirs of molecular gas, have been deduced in several objects from submillimetre (submm) studies (e.g. Reuland et al. 2004).

* *Herschel* is an ESA space observatory with science instruments provided by European-led Principal Investigator consortia and with important participation from NASA.

Such studies were mainly based on one submm flux measurement and were limited to the highest redshift objects for which the obscured newborn star radiation re-emitted by the ubiquitous cold (30–50 K) dust is redshifted to submm wavelengths. However, quantification of the cold dust emission (e.g. constraining the cold dust temperature) requires sampling the full rest-frame infrared-submm spectral energy distribution (SED) of the studied objects. Earlier far-infrared (FIR) studies failed to provide strong constraints on the FIR properties for relatively large samples of powerful radio-loud AGN because of their small detection fractions and only limited rest-frame FIR wavelength coverage (Heckman et al. 1992; Hes et al. 1995; Meisenheimer et al. 2001; Siebenmorgen et al. 2004; Haas et al. 2004; Cleary et al. 2007).

The *Herschel Space Observatory* (Pilbratt et al. 2010), with its unprecedented FIR sensitivity and wavelength coverage, explored terra incognita (caelum incognitum...) allowing studies which have revolutionized the understanding of the connection between AGN and star formation activity. Several studies utilizing deep X-ray and *Herschel* data revealed that the hosts of moderately luminous radio-quiet AGN out to $z \sim 3$ form stars at rates comparable to the general non-AGN population (Shao et al. 2010; Mullaney et al. 2012; Rosario et al. 2012). For high (radio-quiet) AGN luminosities ($L_X > 10^{44}$ erg s $^{-1}$), Page et al. (2012) reported suppression of star formation, consistent with the expectations from theoretical models, while Harrison et al. (2012) found no clear evidence of suppression of star formation by extending the analyses to samples larger by an order of magnitude. Moreover, at the highest AGN luminosities (in excess of 10^{46} erg s $^{-1}$), recent studies based on decomposition of the IR emission to AGN and star formation contributions, have shown star formation rates (SFRs) of the order of several hundred solar masses per year in the hosts of some of the most powerful radio galaxies (Barthel et al. 2012, - B12 hereafter; Seymour et al. 2012; Drouart et al. 2014) and (radio-quiet) quasars (Leipski et al. 2013, 2014).

In order to quantify the energetics of AGN at the peak of their activity as well as their star formation characteristics, we obtained five-band *Herschel* photometry of the 3CR sample using the *Photodetector Array Camera* (PACS) at 70 and 160 μ m and the *Spectral and Photometric Imaging Receiver* (SPIRE) at 250, 350, and 500 μ m on-board the *Herschel Space Observatory*. The first results, dealing with 3 archetypal objects of that sample were presented in B12. Here we analyse the FIR properties of the complete (flux-limited) sample of objects spanning the redshift range $1 < z < 2.5$. This paper is organized as follows. Section 2 describes the sample selection, the data obtained, and the steps used for measuring flux densities in the five *Herschel* bands. Section 3 addresses the procedure for fitting the observed IR SEDs of the objects. Results are then presented and discussed in Sect. 4 and Sect. 5, respectively, and the paper is briefly summarized in Sect. 6. Throughout this paper we use a flat cosmology with $H_0 = 70$ km s $^{-1}$ Mpc $^{-1}$ and $\Omega_\Lambda = 0.7$, and we follow the conversion in Kennicutt (1998) (which assumes a Salpeter 1955 initial mass function) when deriving SFRs.

2. Data

2.1. Sample selection

With this study, we target the well known, complete flux-limited sample of the brightest ($F_{178 \text{ MHz}} > 10$ Jy), high-redshift ($z > 1$) radio-loud AGN sample in the northern hemisphere: the Revised Third Cambridge Catalogue of radio sources (hereafter 3CR;

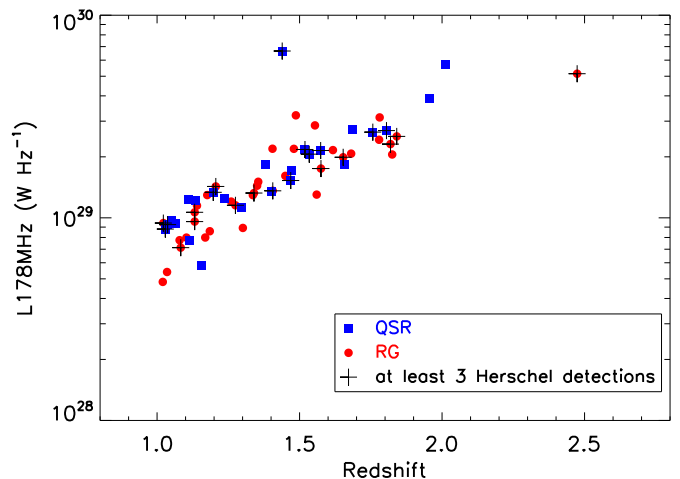


Fig. 1. Observed radio (178 MHz) luminosity as a function of redshift for the 3CR sample considered in this work. Circles (red) indicate radio galaxies, and squares (blue) indicate quasars. The plus symbols mark the objects detected in at least three *Herschel* bands (typically the two PACS and the SPIRE 250 μ m bands).

Spinrad et al. 1985). The extremely high luminosities (Fig. 1) of these double-lobed radio galaxies (RGs) and quasars (QSRs) are produced by some of the most powerful accreting SMBHs. The low-frequency (178 MHz) radio selection ensures no bias with respect to orientation: the steep-spectrum lobes of radio-loud AGN emit optically thin and isotropic synchrotron radiation, making the 3CR sample ideal for testing the orientation-based unification scenario of radio-loud AGN. As shown in Fig. 1, both the RGs and QSRs are homogeneously distributed in redshift. The $z > 1$ 3CR objects show mostly FR II morphologies; this is well-established from, for instance, high-resolution VLA maps. Compact, presumably young, morphologies (O’Dea 1998) are also found within the sample.

The $z > 1$ 3CR sample is (spectroscopically) completely identified using 3 to 5 m-class telescopes in the 1960s–1980s (Spinrad et al. 1985). The objects in the sample almost universally accrete at high Eddington rate, i.e. in quasar-mode (e.g. Best & Heckman 2012). The total number of objects in the $z > 1$ 3CR sample is 64¹. The highest redshift 3CR source is 3C 257 ($z = 2.47$). Two $z > 1$ 3CR sources, 3C 287 and 3C 300.1, have been observed in other *Herschel* observing modes, and thus have been dropped from this work. The remaining 62 sources, 37 RGs and 25 QSRs, comprise the *Herschel* sample studied in this work. An overview of selected properties is provided in Table 1.

The high- z 3CR sample has been observed with many space telescopes (including *Hubble*, *Spitzer*, and *Chandra*; Best et al. 1998; Haas et al. 2008; Leipski et al. 2010; Wilkes et al. 2013); objects from this sample represent landmarks in our study of active galaxies through cosmic time.

2.2. Herschel photometry

The data for this work were obtained as part of our *Herschel* Guaranteed Time project *The Herschel Legacy of distant radio-loud AGN* (PI: Barthel, 38 hours of observations). Five objects (see Table 1) were observed as part of another *Herschel* programme (PI: Seymour). The raw data for these objects were re-

¹ The sample includes two 4C objects, 4C 13.66 and 4C 16.49, which formally match the selection criteria of, and are included in, the 3CR sample.

trieved from the *Herschel Science Archive* (HSA), and the data reduction was performed as detailed below.

2.2.1. PACS

Photometric observations were carried out with PACS (Poglitsch et al. 2010) in the scan-map observational mode, both in the blue ($70\ \mu\text{m}$, $5''$ angular resolution) and in the red ($160\ \mu\text{m}$, $11''$ angular resolution) bands. A concatenated pair of coextensive scan maps at two different orientations was obtained for each source. Data reduction was performed within the *Herschel Interactive Processing Environment* (HIPE, Ott 2010, version 11.0.0), following the standard procedures for deep field observations. Maps were created by employing the high-pass filtering method, using an appropriate source masking step to avoid significant flux losses due to the high-pass filter. A first data reduction resulted in a preliminary map, created after combining the individually (for each scan orientation) processed scan maps. Source masking was performed by hand, using the preliminary created map as an input. This method in particular allowed us to minimize the flux losses of the observed sources (Popesso et al. 2012). The final data reduction and mosaicking were then performed using the mask generated in the previous step.

Photometry (using appropriate aperture corrections) was performed within HIPE, using the *annularSkyAperturePhotometry* task. Apertures of $6''$ and $10''$ radius for PACS blue and PACS red, respectively, were centred on the known radio core position of the object in the map. PACS maps suffer from correlated noise, thus pixel-to-pixel variations cannot yield robust photometric uncertainties. Instead, we opted for the well-established procedure of placing apertures at random positions on the sky (Lutz et al. 2011; Popesso et al. 2012). Following Leipski et al. (2013), we placed 500 apertures of $6''$ (for blue) and $10''$ (for red) radii at locations avoiding the noisy edges of the map, requiring that the central pixel of the random aperture has at least 75% of the integration time of that of the source of interest. The resulting distribution of the flux densities measured in these 500 apertures was then fitted with a Gaussian, and the sigma value of the Gaussian was taken to be the 1σ photometric uncertainty of the map. Measured flux densities and associated 1σ uncertainties, together with 3σ upper limits for the non-detections are provided in Table 2. The PACS photometric uncertainties provided in Table 2 do not include the 5% uncertainty on the absolute flux calibration (Balog et al. 2013). Postage stamps of the resulting PACS maps, centred on the radio position of the objects, are included in Appendix E.

2.2.2. SPIRE

SPIRE (Griffin et al. 2010) photometric observations were carried out in small scan-map observational mode, at 250 ($18.2''$ angular resolution), 350 ($24.9''$ angular resolution) and $500\ \mu\text{m}$ ($36.3''$ angular resolution). Data reduction was performed in HIPE following standard procedures for SPIRE data. Source extraction on the fully reduced map was performed using the *sourceExtractorSussexextractor* task (Savage & Oliver 2007). Extracted sources located within half the Full Width at Half Maximum (FWHM) of the given SPIRE array (measured from the radio core position of the sources) were selected as tentative detections.

While SPIRE does not suffer from correlated noise, SPIRE observations are dominated by confusion noise, of the order of

$6\text{--}7\ \text{mJy beam}^{-1}$, as estimated from deep extragalactic observations (Nguyen et al. 2010). Our adopted procedure for the determination of the photometric uncertainties in the SPIRE maps is fully described by Leipski et al. (2013), which in turn follows the procedures presented by Elbaz et al. (2011) and Pascale et al. (2011). Initially, an artificial source free map was created by removing the extracted sources in a SPIRE map from the map itself. Then, the pixel-to-pixel rms in this source free map was calculated using a box centred on the nominal position of the target object. The size of the box was chosen as a compromise between avoiding the noisy edges of the SPIRE map and obtaining proper statistics of the immediate environment of the target object.

As indicated in Table 2, three SPIRE detections are formally below the estimated 3σ values. These particular measurements were included in the subsequent analyses because, upon visual inspection, they showed obvious emission at the known position of the target object. The availability of ancillary multi-wavelength data at shorter wavelengths (to check for source confusion), and the understanding of the overall shape of the object's SED, further support the inclusion of these flux densities in the subsequent analyses. While the formal signal-to-noise ratio of one of these three detections is very close to three, the other two detections do not reach this ratio only because the associated SPIRE maps are less clean than other maps in the sample, leading to significantly larger photometric uncertainties. The SPIRE $500\ \mu\text{m}$ photometry should be considered tentative because the beam at this particular wavelength is large, and undetected sources in the region surrounding the AGN may contribute to the measured flux density. The SPIRE photometric uncertainties provided in Table 2 do not include the 4% uncertainty on the absolute flux calibration (Bendo et al. 2013). Postage stamps of the resulting SPIRE maps, centred on the radio position of the objects, are included in Appendix E.

2.3. Supplementary Data

The FIR photometry of all 3CR sources in our work was supplemented with MIR photometry obtained with the *Spitzer Space Telescope* (Werner et al. 2004) during three *Spitzer* GT observing programmes (PI: G. Fazio) in six bands, using the instruments IRAC (Fazio et al. 2004), IRS-16 peak-up array (Houck et al. 2004), and MIPS (Rieke et al. 2004). Details on the *Spitzer* data reduction and photometry have previously been published by Haas et al. (2008). Table 2 lists the *Spitzer* photometry. When available, additional $850\ \mu\text{m}$ data were collected from the literature. The $850\ \mu\text{m}$ emission in quasars can be heavily contaminated by synchrotron contribution (see Sect. 3.3). The quasar $850\ \mu\text{m}$ thermal flux densities utilized in this work were taken from Haas et al. (2006). To obtain the $850\ \mu\text{m}$ thermal flux densities of quasars, Haas et al. (2006) extrapolated the synchrotron contribution at $850\ \mu\text{m}$ using the measured radio core flux densities, and subtracted it from the total flux density at $850\ \mu\text{m}$. Table 3 lists the radio galaxy and quasar thermal submm flux densities used in this work.

3. Spectral energy distributions

3.1. Fitting components

The estimation of physical properties for the active galaxies was performed using an SED fitting technique. Our fitting routine is based on a combination of several distinct components, responsible for the emission from active galaxies in different wavelength

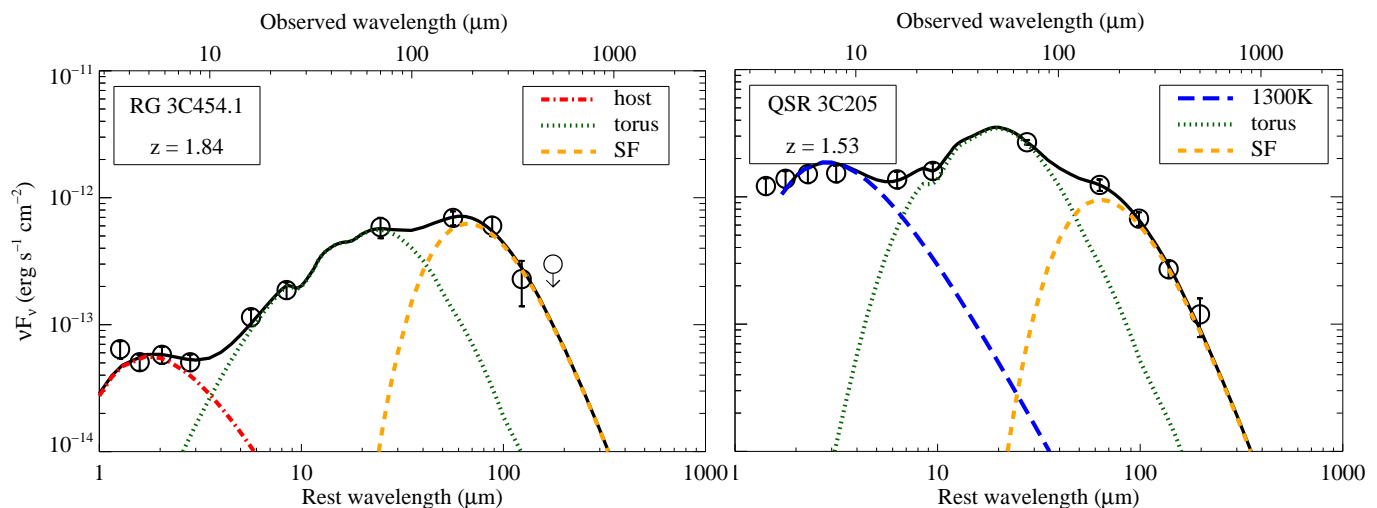


Fig. 2. IR spectral energy distributions (SEDs, solid black) for two representative objects from this work. Open circles show the photometric data. Error bars correspond to 1σ photometric uncertainties. Arrows indicate 3σ upper limits. Left panel: 3C 454.1, a radio galaxy at $z=1.84$. The three components used to fit the SEDs of radio galaxies account for emission from host galaxy (old) stars (dash-dotted red), from an AGN-heated torus (dotted green), and from dust heated by star formation (dashed yellow). Right panel: 3C 205, a quasar at $z=1.53$. The multi-component approach used to fit quasars accounts for emission from hot (1300 K) dust (long-dashed blue), from the AGN-heated torus (dotted green) and from the star formation heated dust (dashed yellow).

regimes. Below, we describe this multi-component approach of fitting the observed IR SEDs.

The presence of circumnuclear dust surrounding the broad line regions in AGN and blocking their UV/visible emission is central to orientation-based unification of powerful FR II radio galaxies and quasars (Barthel 1989; Antonucci 1993). Given its proximity to the AGN, the emission from this AGN-illuminated warm dust peaks at rest-frame MIR (10–40 μm) wavelengths (e.g. Rowan-Robinson 1995). *Spitzer* photometric and spectroscopic data have shown that the majority of high- z 3CR objects are luminous MIR emitters (Haas et al. 2008; Leipski et al. 2010), with observed MIR luminosities $L_{15\mu\text{m}}$ much higher than $8 \times 10^{43} \text{ ergs s}^{-1}$, the value separating hidden quasars from mid-IR weak radio galaxies at intermediate redshifts (Ogle et al. 2006). There exists broad agreement that the AGN-heated nuclear dust is mainly located in clumps which are distributed in a toroidal pattern altogether referred to as the AGN torus (e.g. Nenkova et al. 2002; Kuraszekiewicz et al. 2003; Hönig et al. 2006; Schartmann et al. 2008). To account for the emission from the AGN heated dust, we chose the library of torus models from Hönig & Kishimoto (2010). The parameters considered when creating this library include the (1) radial dust distribution of dust clumps; (2) geometric thickness of the torus; (3) number of clumps along an equatorial line of sight; (4) optical depth of the individual clumps; and (5) outer radius of the torus. There are 240 sets of parameters in the library, each computed for seven viewing-angles ranging from face-on ($i = 0^\circ$) to edge-on ($i = 90^\circ$) in steps of 15 degrees, resulting in a total of 1680 torus models. Detailed information on the model parameters and the adopted strategy in generating the tori SEDs is provided by Hönig & Kishimoto (2010). In addition to the parameters listed above, the overall flux normalization of the model is another free parameter throughout the fitting procedure (outlined below).

The rest-frame FIR emission (40–500 μm) is largely generated by cold dust, heated by star formation on kpc-scales in the AGN host (e.g. Rowan-Robinson 1995; Schweitzer et al. 2006; Netzer et al. 2007). Following these authors, we interpret any

FIR emission (in excess of the emission of the AGN-heated dust) as being powered by star formation, and we represent it with an optically thin modified blackbody component, i.e., a blackbody modified by frequency-dependent emissivity, given by

$$S_\nu \propto B_\nu(T)\nu^\beta. \quad (1)$$

We reduce the number of free parameters in this component by fixing the dust emissivity index β to a typical value of 1.6 as found in studies of high- z AGN (e.g. Beelen et al. 2006). The remaining two free parameters here are the cold dust temperature and the flux normalization of the modified blackbody component. The use of a modified blackbody, as opposed to starburst templates (e.g. Drouart et al. 2014), might slightly underestimate the star formation luminosities because one misses the starburst MIR emission, but offers the unique possibility of constraining the cold dust temperatures.

The two components described above feature in the SED fitting of both radio galaxies and quasars. We include additional SED components to the fitting depending on the type of the studied object. For radio galaxies, we added a blackbody component peaking in the near-IR to account for the emission from the old stellar population in the AGN host (e.g. Seymour et al. 2007). The temperature of the blackbody and its flux normalization are the two free parameters for this SED component. For quasars, we added a blackbody component to account for the hot (graphite) dust close to the sublimation temperature. This component is often empirically required to fit the observed SEDs of quasars (e.g. Mor & Netzer 2012; Leipski et al. 2013). Following these authors, we fixed the temperature of the blackbody to 1300 K, leaving its flux normalization as the only free parameter during the fitting. Such a component is also needed in the fitting of the SEDs of a few radio galaxies (see also B12) whose observed photometry in the NIR/MIR could not be well represented with the components described above. These radio galaxies, indicated in Table 4, might be viewed along lines of sight at which the nuclear region is only partly obscured, thus resulting in somewhat elevated MIR luminosities. The inclusion of the hot dust component to the SEDs of some of the radio galaxies might lower

the estimates of the mass of the evolved stellar populations, but this is outside the scope of this work. For the quasars we also considered an additional power-law component representing the emission from an accretion disk in the UV/visible. However, as demonstrated in Appendix A, the inclusion of this power-law component had little influence on the results obtained from the FIR part of the SED, therefore it was excluded from the fitting procedure.

3.2. Fitting procedure

While our physically motivated fitting approach results in a close approximation of the observed SEDs of the sample objects, it is not primarily designed to yield precise models of their SEDs. In particular, we are not interested in constraining the properties of the dusty torus with our multi-wavelength broad-band photometry. This kind of analysis remains challenging even at lower redshifts (e.g. Ramos Almeida et al. 2009). Torus models are used to separate AGN-heated dust emission (peaking in MIR) from star-formation-heated dust emission (peaking in FIR), and to determine for the first time the star-formation-dominated FIR energetics of the high- z 3CR sources. When fitting the observed SEDs of our objects, we used a chi-square minimization technique based on the MPFIT routine (Markwardt 2009). In practice, we started with a torus model from the library of Hönig & Kishimoto (2010) and added a linear combination of the remaining SED components (depending on the object type) to minimize the overall chi-square. We repeated the procedure for each torus model in the library.

Example best-fit SEDs, along with their individual SED components, are shown in Fig. 2. At the redshifts of our sample, the PACS 70 μm band is crucial in our adopted fitting approach, as it strongly constrains the longer wavelengths of the torus emission. On the other hand, the SPIRE 250 μm band is the most important measurement for constraining the component representing the cold dust emission. Therefore, our fitting approach was applied to all objects that are detected in at least three *Herschel* photometric bands (typically the three shortest *Herschel* bands). These objects are homogeneously distributed in the redshift range ($1 < z < 2.5$) studied in this work (Fig. 1). Best-fit SEDs for these objects, together with images centred on the radio positions of the AGN, are presented in Appendix C and in Appendix E, respectively. Occasional SED mismatches at observed-frame 16 μm and/or 24 μm are most probably due to luminous polycyclic aromatic hydrocarbon emission and/or the 10 μm silicate absorption (Haas et al. 2008; Leipski et al. 2010). At FIR wavelengths, the fixed β approach may be the main reason behind the failure of the fitting routine to exactly reproduce some SPIRE data points.

The physical parameters constrained by our fitting method include IR star formation and IR AGN luminosity, and the temperature and mass of the cold dust component (Fig. 3, Table 4). Uncertainties in the derived parameters were calculated by re-sampling the observed SEDs, allowing the individual photometric measurements to vary within their 1σ ranges of uncertainty. More precisely, we generated 100 mock observed SEDs and studied the distributions of the parameters derived from the corresponding best fits. We inspected the best fits to the mock SEDs to confirm their overall quality in the different wavelength regimes. From the distributions, we retained the median values as the best estimates of the parameters, and the 16th-84th percentile ranges as their associated uncertainties (which in case of a Gaussian distribution would correspond to $\pm 1\sigma$ values).

For objects with fewer than three *Herschel* detections, we estimated upper limits for the IR star formation and IR AGN luminosities using two different approaches. In the first approach, we fitted the (longer wavelength) *Herschel* upper limits using a modified blackbody with fixed $\beta = 1.6$ value and fixed cold dust temperature ($T_{\text{dust}} = 37$ K), typically found from the fits of the objects detected in at least three *Herschel* bands (see below). We then integrated under the blackbody component to estimate upper limits for the star formation luminosities. In the second approach, we took the 70/160/250 μm upper limits as tentative detections, and estimated upper limits for the star formation luminosities using the procedure adopted for the objects detected in at least three *Herschel* bands. Both approaches yielded similar results (within 10%) for the star formation luminosities, but we retained the second approach because it allowed us to estimate the IR AGN luminosities for objects with only PACS 70 μm detections. Best-fit SEDs for objects with fewer than three *Herschel* detections, together with images centred on the radio positions of the AGN, are presented in Appendix D and in Appendix E, respectively. Systematically demanding three *Herschel* detections when fitting the observed photometry regardless of redshift means that the FIR results for the objects detected in only the two PACS bands are treated as upper limits. However, depending on the object's redshift, the PACS 160 μm band alone may probe the peak of the cold dust emission, allowing robust constraints for the physical parameters estimated in this work.

3.3. Synchrotron contribution

Earlier submillimetre and millimetre studies of high-redshift 3CR sources presented clear evidence for a synchrotron contribution to the observed flux densities (van Bemmelen et al. 1998; Archibald et al. 2001; Willott et al. 2002; Haas et al. 2006). While negligible for radio galaxies, extrapolation from core radio data shows that synchrotron emission can account for up to 80% of the observed submm flux densities from quasars (Haas et al. 2006). However, the longest rest-frame wavelengths probed by the SPIRE 500 μm band in our study are ~ 200 μm : emission at these wavelengths is completely dominated by dust and therefore free from any synchrotron contribution. The only exception is 3C 418. This source appears to be flat-spectrum-core-dominated (in an otherwise steep-spectrum selected sample), and as such its FIR SED is clearly dominated by non-thermal (synchrotron) radiation from its core. The power-law like IR SED of this source is shown in Appendix C. 3C 418 was removed from the subsequent analyses.

4. Results

4.1. Detection statistics

The *Herschel* detection rate throughout our sample ranges from 67% in the PACS 70 μm band to 13% in the SPIRE 500 μm band. In particular, 7 objects have robust detections in all five *Herschel* bands. Furthermore, a total of 24 objects are detected in at least three *Herschel* bands, most importantly in the SPIRE 250 μm band, which for the highest redshift of our sample (3C 257: $z = 2.47$) corresponds to ~ 70 μm rest-frame emission². Excluding 3C 418 from these 24 objects, results in 13 radio galaxies and 10

² For the median redshift of our sample, ($z_{\text{med}}=1.38$), the SPIRE 250 μm band samples the peak (~ 100 μm) of the typical cold dust SED, allowing strong constraints on the modified blackbody component used in the fitting approach.

Table 3. Objects with significant thermal submillimetre flux densities.

Object	Thermal $F_{850\mu\text{m}}$ (mJy)	Reference
3C 191	2.95	1, 2
3C 257	5.40	3
3C 280.1	2.48	1, 2
3C 298	7.25	1, 2
3C 368	4.08	3
3C 432	6.33	1, 2
3C 470	5.64	3
4C 13.66	3.53	3

References. (1) Willott et al. (2002); (2) Haas et al. (2006); (3) Archibald et al. (2001).

quasars. The *Spitzer* detection rate throughout our sample ranges from 94% in the IRS 16 μm and MIPS 24 μm bands to 100% in the IRAC 5.8 μm band. Comments on selected individual objects are included in Appendix B.

4.2. Physical properties obtained from the SED fitting

Studies investigating the cold dust temperatures in high- z objects prior to *Herschel* were often uncertain because they relied heavily on observations in a single photometric broadband (e.g. Benford et al. 1999; Beelen et al. 2006). In our current study, cold dust temperatures estimated for the FIR-detected objects range from ~ 25 to ~ 45 K (Fig. 3, Table 4). Radio galaxies and quasars span the same range in cold dust temperatures. This range is similar to that obtained for $z > 5$ quasars (Leipski et al. 2014) and to that estimated for distant submm galaxies (e.g. Magnelli et al. 2012). Similarly to Leipski et al. (2013), the inclusion of the 1300 K hot dust component in the SED fitting lowers the estimates of the cold dust temperatures by ~ 5 K. By including the hot dust component, we preferentially select torus models that emit more of their energy at longer wavelengths. As a consequence, the cold dust components are also shifted to colder temperatures.

Central to the subsequent discussion are the star formation luminosities, L_{SF} , which we computed (or estimated upper limits) by integrating the best-fit modified blackbody components from 8 μm through 1000 μm . Figure 3 shows the distribution of L_{SF} for the radio galaxies and quasars detected in at least three *Herschel* bands. Both types of objects show similarly broad distributions, with many objects having $L_{\text{SF}} > 10^{12} L_{\odot}$, characterizing them as ultra-luminous infrared galaxies (ULIRGs) (see also Table 4). The median star formation luminosities of the RGs and QSRs plotted in Fig. 3 are $2.0 \times 10^{12} L_{\odot}$ and $2.6 \times 10^{12} L_{\odot}$, respectively. Converting the star formation luminosities into SFRs using the calibration derived by Kennicutt (1998) gives $100 M_{\odot} \text{ yr}^{-1} < \text{SFR} < 1000 M_{\odot} \text{ yr}^{-1}$, consistent with SFRs obtained for typical submm galaxies (SMGs) at comparable redshifts (e.g. Magnelli et al. 2012).

To compute the IR luminosities of the components powered by the AGN, L_{AGN} , we integrated the best-fit torus component for the RGs and the sum of the best-fit hot dust and torus component for the QSRs³ between 1 μm and 1000 μm . Figure 3

³ A few RGs also require an additional hot dust component to better fit their observed photometry. The computation of L_{AGN} for these objects takes into account this component as well.

shows that the RGs and QSRs occupy different ranges in the distributions of L_{AGN} , with the distribution for QSRs shifted to higher values compared to that for RGs. Haas et al. (2008) already established this result by investigating the (energetically important) rest 1.6–10 μm wavelength range for the high- z 3CR objects, finding the QSRs to be, on average, 3–10 times more luminous than RGs. We confirm their finding by including rest-frame wavelengths longer than 10 μm . The median IR AGN luminosities of the RGs and QSRs plotted in Fig. 3 are $3.7 \times 10^{12} L_{\odot}$ and $1.1 \times 10^{13} L_{\odot}$, respectively.

As outlined in previous sections, we attribute the FIR emission in excess of the AGN-powered dust emission to emission from star-formation-heated dust. Figure 4 shows L_{SF} as a function of L_{AGN} for all objects in our sample. The presence/absence of correlation between these two parameters depends on both redshift and AGN luminosity, and is still debated in the literature (Lutz 2014). Given the data, and taking into account only the FIR-detected objects, the two plotted parameters show at most a weak correlation, in part introduced by the dependence of both L_{SF} and L_{AGN} on redshift. Moreover, the numerous upper limits, together with the fact that both parameters span only a limited range (~ 2 orders of magnitude), make it difficult to establish any such correlation (or lack of) in our sample. Nevertheless, we observe a range of L_{SF} from weak (if not absent) to very strong, coeval with the growth of the black hole. Figure 4 also shows that the hosts of even the strongest AGN can have significant star formation activity, unlike the trends found by Page et al. (2012) for radio-quiet AGN. In general, the total IR emission from the 3CR AGN is predominantly AGN powered, despite the frequently accompanying strong star formation activity.

We estimated the mass of the FIR emitting dust component, M_{dust} , using

$$M_{\text{dust}} = \frac{S_{250\mu\text{m}} D_L^2}{\kappa_{250\mu\text{m}} B_{\nu}(250\mu\text{m}, T_{\text{dust}})}, \quad (2)$$

where $S_{250\mu\text{m}}$ is the flux at 250 μm rest-frame found from the best-fit, D_L is the luminosity distance, $\kappa_{250\mu\text{m}}$ is the dust absorption coefficient at 250 μm ($\kappa_{250\mu\text{m}} = 4 \text{ cm}^2 \text{ g}^{-1}$ from the models of Draine 2003), and $B_{\nu}(250\mu\text{m}, T_{\text{dust}})$ is the value of the Planck function at the corresponding rest-frame wavelength and temperature. Results are shown in Table 4. Given that the RGs and QSRs in our sample cover roughly the same redshift range and show similar star formation properties, it is no surprise that their cold dust masses are comparable as well. More interestingly, the masses of the cold dust component in the hosts of radio-loud AGN detected in at least three *Herschel* bands are comparable to those obtained for SMGs at redshifts similar to those of our sample (e.g. Santini et al. 2010). The dust masses of radio-loud AGN provide clues to the triggering of the starburst event (and also that of the black hole activity, Tadhunter et al. 2014). Given that the high- z SMGs are likely undergoing strong merger-induced starburst events (e.g. Kartaltepe et al. 2012), their similar dust content suggests that that FIR-luminous radio-loud AGN also build up their stellar mass in major gas-rich mergers.

4.3. Median SEDs

The best-fit SEDs for the objects detected in at least three *Herschel* bands are shown in Appendix C. The SEDs show a considerable range of shapes and absolute scaling, with all QSR (and a few RG) SEDs peaking at wavelengths around 20 μm , and most RG SEDs peaking at longer wavelengths. Furthermore, the SEDs show that the AGN-powered and star-formation-powered

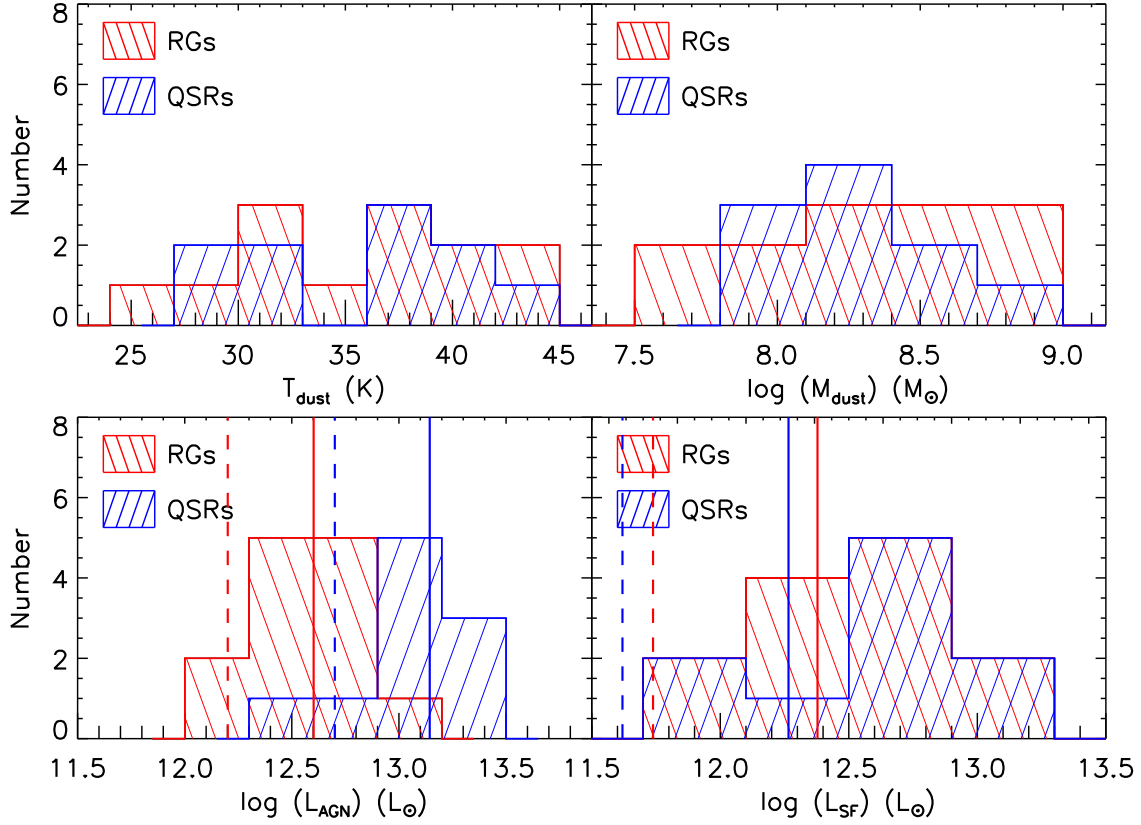


Fig. 3. Distributions of individual physical parameters obtained from the SED fits, for radio galaxies (red) and quasars (blue). The values plotted are those for the objects detected in at least three *Herschel* bands. Upper left panel: temperature of the cold dust component emitting in the FIR, T_{dust} . Upper right panel: mass of the FIR emitting cold dust component, M_{dust} . Lower left panel: AGN-powered IR luminosity, L_{AGN} . Lower right panel: star-formation-powered IR luminosity, L_{SF} . The vertical lines in the lower panels correspond to the average values of the FIR-detected (solid lines) and non-detected (dashed lines) stacked subsamples discussed in Sect. 4.4.

dust emission switch dominance typically at $50 \mu\text{m}$, (but this can happen at all wavelengths between 35 and $65 \mu\text{m}$). Given that all SEDs were computed on the same rest-frame wavelength grid, we created median SEDs for the two types of objects to prevent the most extreme objects dominating the average SEDs. When creating the median SEDs, we refrained from applying any normalization, in order to preserve the absolute luminosities of the individual SEDs. The median⁴ SEDs are shown in Fig. 5.

The median SEDs of RGs and QSRs differ strongly at rest-frame $3\text{--}10 \mu\text{m}$, with the QSRs being a few times more luminous than the RGs. Such an observational difference in this wavelength regime has already been explained by Haas et al. (2008) in the context of unification by orientation. In this scenario, the observed luminosity differences result from viewing the QSRs and RGs along different angles, such that the hot inner regions of the dusty torus are observed directly in the case of QSRs but are obscured in the case of RGs. As found by Leipski et al. (2010), similar observational differences correlate with orientation indicators, such as the radio core dominance. The median SED of RGs can therefore be viewed as the median SED of reddened QSRs (Haas et al. 2008; Leipski et al. 2010). At rest-

frame wavelengths between 10 and $40 \mu\text{m}$, the median RG and QSR SEDs still show a considerable anisotropy, with the QSRs being a factor of two more luminous compared to the RGs at $20 \mu\text{m}$. At rest-frame FIR wavelengths ($\gtrsim 40 \mu\text{m}$), however, the median RG and QSR SEDs appear to be remarkably similar both in shape and absolute scale, arguing for, on average, similar star formation properties for the hosts of both types of AGN.

Figure 5 also shows the average SED for the subsample of the $z \sim 2$ star-forming galaxies from Kirkpatrick et al. (2012). This average SED is composed of 30 (U)LIRG galaxies, initially selected based on their $24 \mu\text{m}$ flux density ($F_{24\mu\text{m}} \gtrsim 100 \mu\text{Jy}$), for which good multi-wavelength coverage is available throughout much of the IR regime. Representing the star-formation-heated cold dust emission with a modified blackbody, Kirkpatrick et al. (2012) estimate the average SFR and cold dust temperature of these galaxies to be $344 \pm 122 M_{\odot} \text{ yr}^{-1}$ and $28 \pm 2 \text{ K}$, respectively. Comparing these (U)LIRG numbers to those obtained for the FIR-detected 3CRs in our work, we find comparable SFRs but on average higher cold dust temperatures. Furthermore, Fig. 5 confirms the marked difference between the (U)LIRGs and 3CRs in the NIR/MIR luminosity: while the $z \sim 2$ star-forming galaxies are characterized by pronounced polycyclic aromatic hydrocarbon (PAH) features, the powerful emission from the warm dusty torus completely outshines these features in the MIR SED of the 3CR host galaxies. Finally, the average stellar mass of the

⁴ The QSRs median SED is given only for rest-frame wavelengths longer than $2 \mu\text{m}$ because the emission at wavelengths shorter than $2 \mu\text{m}$ is dominated by the hot accretion disk, which was not included in our SED fitting (as explained in Appendix A).

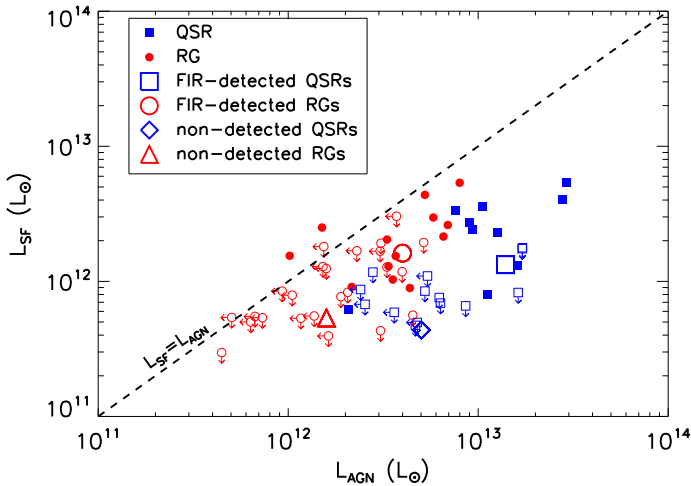


Fig. 4. IR emission from star-formation-heated cold dust, L_{SF} , versus IR emission from AGN-powered dust, L_{AGN} , for radio galaxies (filled red circles) and quasars (filled blue squares). Upper limits have been estimated as explained in the text. The large empty symbols correspond to the subsamples of FIR-detected RGs (circle) and QSRs (square), and non-detected RGs (triangle) and QSRs (diamond) discussed in Sect. 4.4. The dashed line marks $L_{\text{SF}} = L_{\text{AGN}}$.

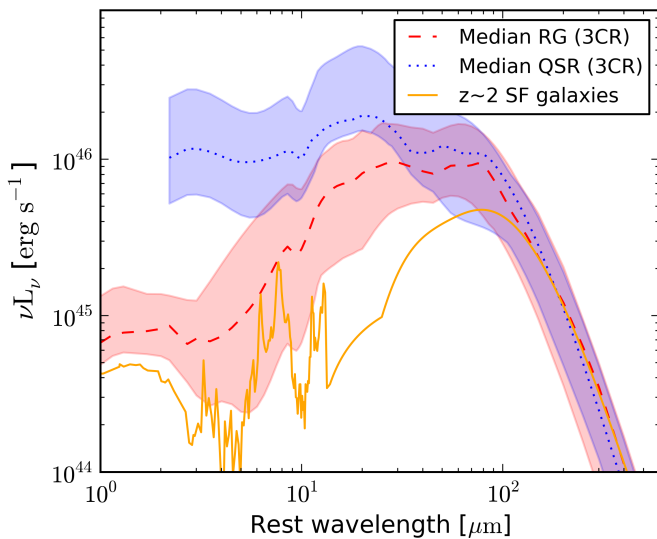


Fig. 5. Median spectral energy distributions (SEDs) for the radio galaxies (dashed red) and quasars (dotted blue) detected in at least three *Herschel* bands, and for $z \sim 2$ star-forming galaxies (solid yellow) from Kirkpatrick et al. (2012). Shaded areas, red for radio galaxies and blue for quasars, correspond to the associated 16th-84th percentile ranges.

$z \sim 2$ star-forming galaxies is a factor of ~ 3 smaller than that of the RG hosts as seen from the offset in the respective SEDs at around $1.6 \mu\text{m}$. While AGN contamination to the $1.6 \mu\text{m}$ is not accounted for in this discussion, the very steep median SED of radio galaxies between 4 and $6 \mu\text{m}$ suggests that any contribution from hot dust to the $1.6 \mu\text{m}$ flux is negligible. AGN contamination at $1.6 \mu\text{m}$ likely is present in individual cases, but does not appear to be crucial when discussing average properties. Overall, the comparison between the 3CR and the Kirkpatrick et al. (2012) sample shows that massive galaxies in the high- z Universe may be actively forming stars regardless of whether their supermassive black holes are accreting or not.

Table 5. Results from the SED fitting of the stacked subsamples.

Subsample	$\log(L_{\text{AGN}}(L_{\odot}))$	$\log(L_{\text{SF}}(L_{\odot}))$
FIR-detected RGs	12.6	12.2
non-detected RGs	<12.2	<11.7
FIR-detected QSRs	13.2	12.1
non-detected QSRs	12.7	<11.6

4.4. Stacking of non-detected objects

In addition to probing the general properties of the objects that are individually detected in at least three *Herschel* bands, we attempt a stacking analysis to extract an average signal for the objects which lack significant emission in the *Herschel* bands. For convenience, we refer to the former objects as FIR-detected, and to the latter as non-detected. Our aim is to discuss average properties for each radio-loud AGN type, therefore we split the non-detected objects into RGs and QSRs, respectively. In order to retain decent number statistics in the two subsamples, we decided not to further divide the RGs and QSRs in redshift bins, despite the considerable redshift range of our sample. In practice, we take the non-detected objects to be those that are detected in at most one, namely the PACS $70 \mu\text{m}$ band, which given the redshifts of our sources often probes the peak emission from the dusty torus. Several RGs and QSRs were not included in the stacking analysis owing to the presence of potentially confusing sources in the corresponding maps, close to the known radio position of the object in question. Furthermore, two RGs (3C 252 and 3C 267) with a strong detection in only the PACS $70 \mu\text{m}$ band were not included in the stacking because they are inconsistent with forming a single population with the objects which have no *Herschel* detections. As a result, stacking was performed on subsamples of 12 RGs and 6 QSRs with median redshifts of $z_{\text{med}}=1.44$ and $z_{\text{med}}=1.27$, respectively. The objects entering the subsamples are flagged in Table 4. For comparison, we also selected two subsamples from the FIR-detected objects: a subsample with 13 RGs ($z_{\text{med}}=1.34$) and another one with 8 QSRs ($z_{\text{med}}=1.52$; 3C 298 and 3C 318, sources with strongly emitting nearby objects, were not taken into consideration).

We stacked equal areas extracted from the individual *Herschel* maps, centred on the known radio position. Photometry on the stacked map was performed following the same procedures as adopted in the case of the individually detected objects (Sect. 2). We examined the diversity within the given subsample by bootstrapping with 1000 realizations. In practice, from the original subsamples identified above, for each bootstrapping realization we selected a random subsample (with the same number of objects, allowing for repetitions), stacked the *Herschel* maps, and performed the photometry. The centroid and the dispersion of the resulting distribution were taken to be the mean flux density of the on-source stack and its associated uncertainty. Additionally, we stacked random positions in order to inspect the overall significance of the on-source stacked signal. If the mean value of the on-source stack distribution was at least three times larger than the mean value of the corresponding background stack distribution, we concluded that the on-source signal is significant. In cases of a non-significant signal, we took three times the mean value of the background stack distribution to be our on-source stack upper limit value.

The mean stacks for the four different subsamples selected in our study are presented in Fig. 6. The non-detected quasars have a significant stacked signal in only the PACS $70 \mu\text{m}$ band,

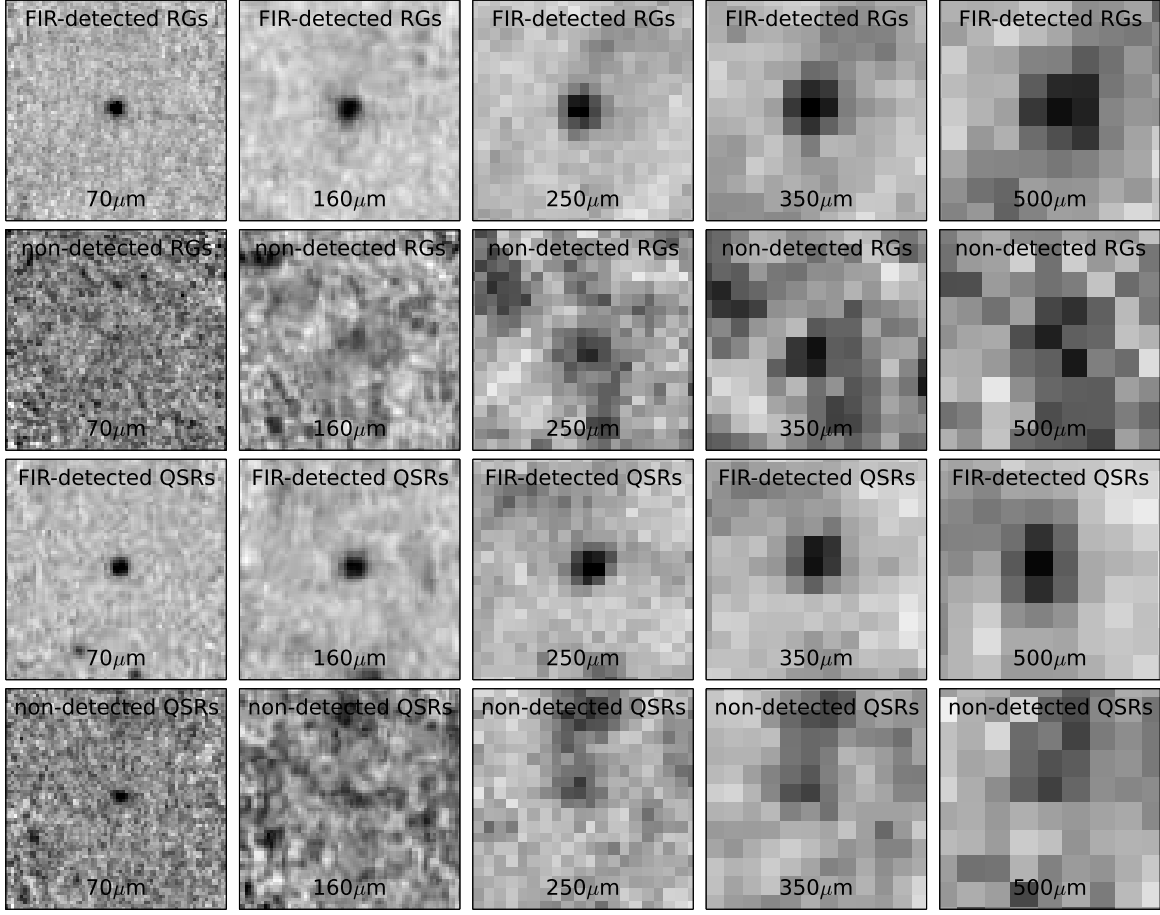


Fig. 6. Stacked images in all *Herschel* bands, for the four subsamples discussed here. From left to right: PACS 70 μm , PACS 160 μm , SPIRE 250 μm , SPIRE 350 μm , and SPIRE 500 μm bands, respectively. From top to bottom: FIR-detected radio galaxies, non-detected radio galaxies, FIR-detected quasars, and non-detected quasars. Each stacked image shown here has dimensions of 2x2 arcmin and is centred on the known radio positions of the objects entering the stack.

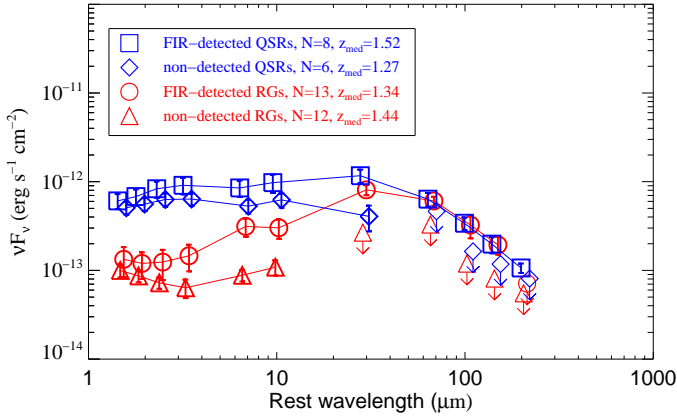


Fig. 7. Spectral energy distributions of stacked subsamples selected from the hosts of the 3CR sources studies here. The four subsamples presented are: FIR-detected radio galaxies (red circles), non-detected radio galaxies (red triangles), FIR-detected quasars (blue squares), and non-detected quasars (blue diamonds). Arrows mark 3σ upper limits as explained in the text.

whereas the non-detected radio galaxies have no significant signal in any of the *Herschel* bands. On the other hand, the FIR-

detected quasars and radio galaxies have significant stacked signals in all, and in all but the SPIRE 500 μm band, respectively. In order to study the full IR SED of a stacked subsample, we calculated mean flux densities in the *Spitzer* bands, where virtually all objects have been individually detected. All obtained average fluxes are in the observed frame: these were transferred to the rest-frame, using the median redshift of the corresponding subsample. The SEDs of the stacked subsamples are shown in Fig. 7.

The 1-10 μm SEDs of radio galaxies are composed of emission from an evolved stellar population and from a heavily reddened AGN (Haas et al. 2008). At the rest-frame wavelengths (given the comparable median redshifts of the various subsamples) probed by the two shortest wavelength *Spitzer* bands ($< 2 \mu\text{m}$), the FIR-detected and non-detected subsamples of RGs are similar. Thus, it is likely that the stellar masses of the host galaxies for the two RG subsamples are, on average, similar as well. Identifying differences in the host galaxy stellar masses requires additional NIR photometry, and is outside the scope of this work. At wavelengths between 2 and 10 μm , the SEDs of the two RG subsamples differ from each other. At these wavelengths, AGN-heated hot dust emission appears to be present/absent in the SED of the FIR-detected/non-detected subsample, respectively, reflecting different levels of dust obscuration, as inferred from the diversity in the individual MIR SEDs of RGs (Haas et al. 2008). Particularly interesting is the non-

significant stacked signal for non-detected RGs at rest-frame $30\ \mu\text{m}$, which could indicate that the two subsamples have different intrinsic AGN luminosities. Indeed, fitting the SEDs following the routine taken in Sect. 3 gives (at least) a factor of two difference between the estimated L_{AGN} in the two RGs subsamples (Table 5, Fig. 4). A clear difference between the SEDs of the two subsamples of RGs is observed at rest-frame wavelengths longer than $60\ \mu\text{m}$, suggesting marked differences in the star formation properties of the two subsamples. This results in (at least) a factor of three difference between the estimated SFRs in the two RGs subsamples (Table 5, Fig. 4). The SEDs of the two QSR subsamples generally follow the same trends as those observed for the RG subsamples. While the non-detected QSRS could overall be at the fainter end of the QSR population, the most striking difference in the QSR SEDs is at FIR wavelengths, with the FIR-detected QSRS having SFRs (at least) a factor of three higher than the non-detected QSRS. While more analysis is required to pin down the potential differences among the subsamples in wavelengths other than FIR, it is beyond doubt that the formation of new stars can be prodigious in some, but modest or weak in other radio-loud AGN hosts.

5. Discussion

5.1. Star formation in hosts of powerful AGN

Starbursts powering the FIR emission in some hosts of radio-loud AGN have been found at low-to-intermediate redshifts (e.g. Dicken et al. 2010). In the high- z Universe, high levels of star formation in some radio-loud AGN have been estimated using several observational indicators. These include the usage of rest-frame UV spectroscopy to detect huge $\text{Ly}\alpha$ halos surrounding the AGN (e.g. Villar-Martín et al. 1999), submm photometry to probe the cool dust and molecular gas content of AGN hosts (e.g. Archibald et al. 2001; Reuland et al. 2004), and *Spitzer* MIR spectroscopy to detect strong PAH features (e.g. Rawlings et al. 2013). The latter, however, are seen only in rare cases because the AGN-powered hot/warm dust emission in powerful radio-loud AGN hosts usually outshines the PAH emission.

UV/visible data have been used to infer SFRs for several 3CR radio galaxies studied in this work (Chambers & Charlot 1990). These include 3C 065, 3C 068.2, 3C 266, 3C 267, 3C 324, 3C 356 and 3C 368. The ratio between the SFR obtained using the approach taken in this work and the UV/visible SFR ranges between 4 and 40, therefore we conclude that the star formation is often strongly obscured in the UV/visible. This comparison demonstrates that rest-frame FIR data are crucial in quantifying the dust-enshrouded star formation in the hosts of these sources, especially the ones hosting quasars because the emission from the accretion disk complicates the SFRs estimates from UV/visible data. Using *Herschel* data, Seymour et al. (2011) found mean SFRs for $1.2 < z < 3.0$ radio-selected AGN to range between 80 and $581\ \text{M}_{\odot}\text{yr}^{-1}$. Similarly, Drouart et al. (2014) studied a sample of $\sim 70\ 1 < z < 5$ radio galaxies, estimating SFRs of a few hundred to a few thousand solar masses per year. While the authors suggest that the highest values reported in their study are likely overestimated and should be treated as upper limits, the overall idea that the hosts of high- z radio-loud AGN can be prodigious star-formers is consistent with our findings for the hosts of the powerful 3CR objects. A crucial point in these analyses is that the high star formation luminosities obtained are coeval with the growth of the SMBHs residing in the nuclei of the host galaxies. As such, these results argue for a scenario whereby on average the SMBH has not

quenched the star formation in the host galaxy, which is at odds with results presented by Page et al. (2012). A series of coeval episodes of strong star formation and black hole activity may have formed the massive host galaxies and their massive black holes (see B12).

The SFRs estimated for the FIR-detected radio-loud AGN are comparable to those obtained for SMGs at similar redshifts (e.g. Magnelli et al. 2012). Other parameters, such as the temperatures and masses of the cold dust component and total stellar masses agree with each other, at least on average, as well (Santini et al. 2010; Michałowski et al. 2012; Swinbank et al. 2014). It is widely thought that high- z SMGs form stars in starburst events, induced as a result of a variety of different processes including mergers and tidal interactions. Radio-loud AGN are known to be at the centres of over-densities in the high- z Universe (e.g. Venemans et al. 2007; Wylezalek et al. 2013). Thus, the merger scenario appears to be an attractive way of producing at least some of the extremely high SFRs estimated in our study. A similar conclusion has been drawn in a study of a few high- z radio galaxies using both *Herschel* and CO observations (Ivison et al. 2012).

Jet-induced star formation, also known as positive feedback, is yet another possible way to trigger high SFRs (e.g. Dey et al. 1997; van Breugel et al. 1998) in hosts of radio-loud AGN. In this scenario, the outgoing radio jet shocks the surrounding interstellar material, which subsequently cools down to form new stars. Recently, based on UV-to-submm templates built with the evolutionary code PEGASE.3, Rocca-Volmerange et al. (2013) showed that the star formation timescales from stellar population synthesis agree well with the ages of the radio episodes for two high- z radio galaxies. Similar studies of larger samples are required to better understand the details of jet-induced star formation.

Despite evidence for strong star formation in the 3CR hosts detected in at least three *Herschel* bands, $\sim 60\%$ of 3CR sources are detected in fewer than three *Herschel* bands, arguing for significantly lower star formation activity in these hosts. While the upper limits in the SPIRE bands still allow energetically significant SFRs of up to $300\ \text{M}_{\odot}\text{yr}^{-1}$ in some of these hosts, the overwhelming majority have SFRs of at most $100\ \text{M}_{\odot}\text{yr}^{-1}$. This raises an important question: what leads to the significantly lower star formation activity in these hosts? If the star formation activity is indeed merger-induced, one possible answer to the above question is that occurrences of minor- and/or gas-poor mergers are likely to lead to relatively low levels of star formation activity. The relevance of the merger scenario in the context of the triggering of starbursts, but also of the AGN activity, has been discussed by Tadhunter et al. (2011). They find that the strongly starbursting radio galaxies in their intermediate-redshift sample have optical morphological features consistent with the idea that they are triggered in major mergers. Another possibility is that we are observing some hosts after the star formation has been quenched (e.g. Farrah et al. 2012). If the AGN activity is responsible for the quenching, then we argue that this negative feedback is not universal, even if it acts over a very short timescale. First, given the strong star formation in the 3CR hosts detected in at least three *Herschel* bands, it is unlikely that the quenching of star formation occurs before the radio-loud AGN phase. Second, quenching taking place during the radio-loud phase is not supported with the finding in Sect. 4.4 that the $< 2\ \mu\text{m}$ rest-frame stacked SEDs of the two RG subsamples are similar. In particular, if star formation in the non-detected RGs is quenched, then they are expected to be brighter than the FIR-detected RGs because the star formation in the latter is heav-

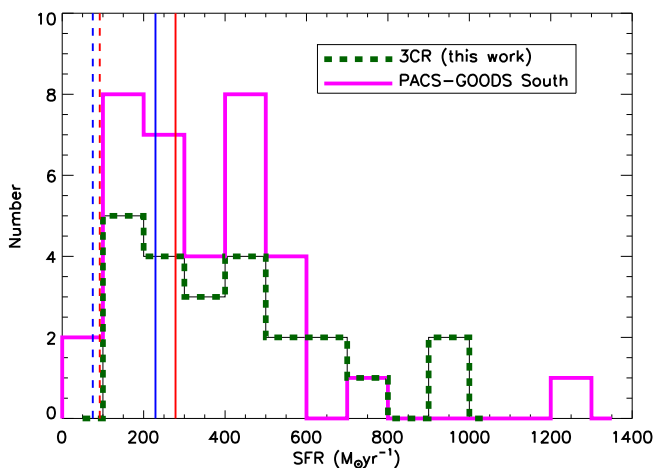


Fig. 8. Comparison of star formation rates of AGN and non-AGN host galaxies. Plotted are the objects detected in at least three *Herschel* bands (dashed green). A comparison sample of objects (solid magenta) is selected from some of the deepest *Herschel* data, from PACS-GOODS South field (Rodighiero et al. 2011). The vertical lines correspond to the average values of the FIR-detected (solid lines) and non-detected (dashed lines) stacked subsamples, discussed in Sect. 4.4.

ily dust obscured. Third, because the radio-loud phase probably marks the end of the AGN phase, it is unlikely that the quenching occurs after the radio-loud phase. To conclude, while the hosts of the quasar-mode radio-loud AGN studied here may have a wide range of star formation rates, it is unlikely that the triggering or quenching of their star formation activity is associated with a uniform scenario met in all objects.

5.2. RG and QSR unification in the FIR

Unification theories of radio-loud AGN (Barthel 1989; Antonucci 1993) ascribe observed differences in the properties of radio galaxies and quasars solely to orientation effects. Using *Spitzer* photometric observations of the sample of 3CR objects studied here, (Haas et al. 2008) (see also the median SEDs from our current work) found the mean 1-10 μm rest-frame radio galaxy SED to be consistent with a sum of an underlying host and a heavily obscured quasar. Unification among the high- z 3CR objects was further corroborated with *Spitzer* spectroscopic (Leipski et al. 2010) and *Chandra* X-ray observations (Wilkes et al. 2013). Our results reveal that the optically thin (i.e. isotropic) FIR emission is similar for radio galaxies and quasars, thus in line with the predictions of radio-loud AGN unification by orientation.

5.3. AGN versus non-AGN host galaxies

It is important to check how the SFRs obtained for the FIR-detected objects in this work compare to those for the non-AGN galaxy population. SFRs in star-forming galaxies are strongly correlated with both stellar mass and redshift (e.g. Elbaz et al. 2007), therefore, the comparison must be made with a sample having a comparable range of stellar mass and redshift. About a dozen 3CR radio galaxies studied in this work have stellar mass estimates primarily based on SED-fitting of visible/NIR (Best et al. 1998) or MIR broad-band photometry (Seymour et al. 2007; De Breuck et al. 2010). The estimated stellar masses range between $1.5 \times 10^{11} M_{\odot}$ and $6 \times 10^{11} M_{\odot}$, and

are not expected to be a function of the redshift/luminosity of the sources (De Breuck et al. 2010). Measurements of stellar masses in high- z quasar hosts are problematic because the strong continuum emission from the accretion disk often outshines their host galaxies. However, assuming that unification of powerful radio galaxies and quasars holds, the masses of quasars and radio galaxies hosts are often taken to be (at least on average) similar (e.g. McLure et al. 2006). Thus, for the discussion below, we assume that the stellar masses of our 3CR hosts range between $1.5 \times 10^{11} M_{\odot}$ and $6 \times 10^{11} M_{\odot}$.

As a control sample of non-AGN galaxies, we selected $1.5 < z < 2.5$ galaxies within the stellar mass range indicated above, whose star-forming properties were estimated from deep PACS data of the GOODS South field (cyan points in Fig. 1 from Rodighiero et al. 2011). The stellar masses of these galaxies were estimated from SED-fitting as explained by Rodighiero et al. (2010). While the majority of the selected galaxies lie on the main sequence of star-forming galaxies, a fraction are located above it, most likely characterized by the starbursting nature of the ongoing star formation (Rodighiero et al. 2011). Figure 8 shows the SFR histograms of the 3CRs and the selected control sample. It is clear that the 3CR FIR-detected objects have, on average, SFRs comparable to those of their equally massive non-AGN counterparts. The majority of FIR-detected objects are thus also located near the main sequence of star-forming galaxies, similarly to what has been found in deep *Herschel*/PACS studies of less powerful, X-ray selected, high- z AGN (Mullaney et al. 2012; Santini et al. 2012; Rosario et al. 2013). In comparison to the FIR-detected objects, the non-detected objects have similar stellar mass but significantly lower SFRs, placing them below the main sequence of star-forming galaxies. We cannot exclude the possibility that the star formation activity in some of these objects has been quenched. Better estimates of the stellar masses of our high- z 3CR sources will allow a more robust statistical study of their exact location with respect to the main sequence of star-forming galaxies.

5.4. Subgalactic versus supergalactic radio sources

The radio morphologies of radio-loud AGN present a unique opportunity to estimate the duration of the AGN episode by assuming a typical speed of radio jet expansion of 10%-20% of the speed of light. The projected radio sizes of our high- z 3CR sources, measured lobe-to-lobe, have been measured from high-resolution radio images. Based on their projected radio sizes, we divided the 3CR sources into two groups, subgalactic (< 30 kpc) and supergalactic radio (> 30 kpc) sources. The subgalactic sources, typically contained within their host galaxies, account for 25% of our high- z 3CR sample. Figure 9 shows the objects' estimated SFRs as a function of their projected radio size. Both the subgalactic and supergalactic FIR-detected 3CR hosts have comparable SFRs. In contrast, the majority of the non-detected objects have larger, i.e. older radio sources. As such, the ratio of FIR-detected versus non-detected objects appears to be a function of projected radio size, changing from 1.3 for subgalactic to 0.5 for supergalactic sources.

There are at least two different effects contributing to the findings presented in Fig. 9. First, the finding that many quiescent galaxies turn up when the radio sources are large is consistent with the fact that star formation depends heavily on the availability of cold gas. Indeed, the process of exhausting the available fuel for star formation has timescales similar to the age of large radio sources. Second, our result that many small radio

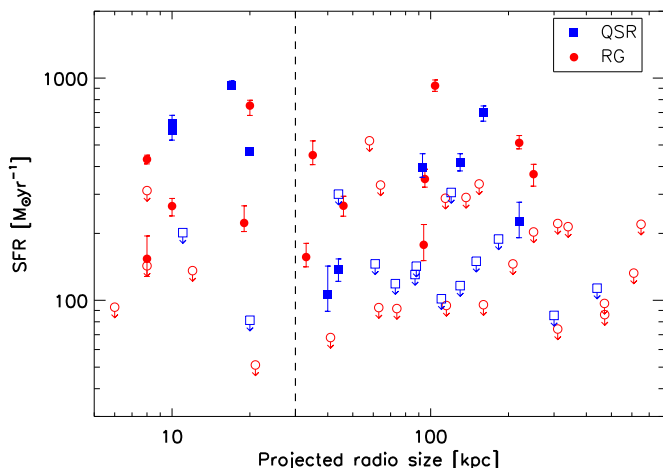


Fig. 9. Estimated star formation rate as a function of projected radio size (measured lobe to lobe) for the 3CR galaxies (red circles) and quasars (blue squares). The dashed line indicates the value taken to differentiate between subgalactic (< 30 kpc) and supergalactic (> 30 kpc) radio sources, respectively. Arrows indicate star formation rate upper limits for objects with fewer than three *Herschel* detections.

sources are hosted by strongly star-forming galaxies is consistent with the observational/theoretical finding that radio jets may induce bursts of star formation (positive feedback, e.g. Silk 2013) in the hosts of high- z (Dey et al. 1997; van Breugel et al. 1998) and low- z radio-loud AGN (Tadhunter et al. 2011; Dicken et al. 2012). Best et al. (1996) found that smaller radio sources show stronger alignment effect⁵ providing further support for the incidence of positive feedback in hosts of small radio sources. A step forward in probing the incidence of positive feedback within the hosts of 3CR sources may be achieved by correlating the ages of the young stellar components and those of the current radio episode, similarly to the study by Rocca-Volmerange et al. (2013). An issue which complicates the overall picture, however, is whether the link between the smaller radio sources and star formation activity is a consequence of an observational bias. Namely, as pointed out by Tadhunter et al. (2011), the interaction between the jet and the host ISM in subgalactic sources may boost the radio emission, leading to a preferential selection of such sources in flux-limited samples, like the 3CR studied here.

5.5. Model fit limitations

Our estimates of the cold dust temperature may suffer from a bias due to the known degeneracy between the cold dust temperature and the dust emissivity index, β : a lower fixed β value will lead to a higher dust temperature. Constraining the emissivity index within our sample is a difficult task because (1) the peak of the dust emission is not well isolated in the SED, and (2) only a few data points probe the Rayleigh-Jeans tail of the dust emission. Because of this, and to limit the number of free parameters throughout the fitting, we fixed the emissivity index to a value of 1.6. However, the detections in all *Herschel* bands, in addition to the availability of submm data, allow β to be constrained for a few selected objects. The β values for these five objects (flagged in Table 4) range from 1 to 2.3, with increased/decreased esti-

⁵ The alignment effect is the co-spatial extent of radio and UV/visible/NIR emission in radio-loud AGN, partly due to the interaction between the jet and the interstellar matter of the host galaxy (McCarthy 1993; Miley & De Breuck 2008).

mated cold dust temperatures for lower/higher β values, respectively. Nevertheless, the star formation luminosities, and consequently SFRs, remain the same (within 10%).

While we attribute the FIR emission to star formation on the scale of the host galaxy, we stress that the FIR emission considered is the excess emission after the AGN-powered torus emission (using the models of Hönig & Kishimoto 2010) has been accounted for. From our SEDs, we concluded that star formation is the dominant process yielding emission at rest-frame wavelengths longer than $\lambda > 50 \mu\text{m}$ (see also Leipski et al. 2013). Nevertheless, should future AGN models demonstrate that the AGN-powered emission continues to dominate at rest-frame wavelengths longer than $\lambda \sim 50 \mu\text{m}$, then our SFR estimates are likely to be upper limits.

6. Conclusions

We present *Herschel* photometry of the complete sample of $z > 1$ 3CR radio galaxies and quasars. The 3CR sample is a flux-limited sample, consisting of some of the most powerful radio-loud AGN accreting in quasar-mode. Combining the *Herschel* photometry with available *Spitzer* data, we performed a full IR SED analysis, separating the contribution from the AGN and from the star formation activity in the host galaxy. We summarize our findings below:

1. About 40% of the studied objects have robust PACS and SPIRE detections, translating into ULIRG-like star formation luminosities, i.e. of the order of SFRs of hundreds of solar masses per year. Such prodigious levels of star formation have recently also been inferred for other high- z radio galaxies (e.g. Drouart et al. 2014). Merger induced and/or jet triggered star formation activity are both possible mechanisms leading to the SFRs obtained for these objects.
2. The SFRs of the FIR-detected objects are comparable to those of mass-matched, non-AGN galaxies, selected from deep *Herschel* surveys. There is no clear evidence that the star formation has been quenched in the hosts of the FIR-detected objects.
3. The total IR (1-1000 μm) emission from the high- z 3CR radio sources is predominantly powered by the AGN, despite the frequently strong starburst activity coeval with the AGN episode. Furthermore, no strong correlation between the AGN- and star formation powered IR luminosities is found.
4. The median SEDs of the FIR-detected objects show that RGs and QSRs are quite different in the MIR, but remarkably similar in the FIR. Thus, while the MIR emission is anisotropic, the FIR emission is isotropic and optically thin. These findings are consistent with the orientation-based unification of radio-loud AGN.
5. Splitting the sample into subgalactic (< 30 kpc) and supergalactic (> 30 kpc) radio sources, the fraction of *Herschel* detected objects is a function of the projected radio size of the sources. In particular, the hosts of subgalactic radio sources are more likely to be detected by *Herschel*, arguing for a possible link between radio size and star formation activity, i.e. jet-induced star formation (positive feedback), or for fading of star formation in mature AGN.

6. Stacking of the *Herschel* non-detected objects reveals a class of MIR/FIR faint objects. While ongoing star formation episodes (at significantly lower levels than those discussed above) cannot be ruled out, star formation has largely ceased in the hosts of these objects. As such, the radio-selected, high- z 3CR hosts appear to be a heterogeneous mixture of MIR/FIR bright and faint objects.

Upcoming instruments with better sensitivity/resolution, such as ALMA, will likely help us pinpoint the exact location of the ongoing star formation in high- z galaxies. This will lead to a further understanding of the interplay between the AGN and star formation activity within high- z AGN hosts.

Acknowledgements. The authors acknowledge the expert referee for useful comments which improved the paper, and thank Giulia Rodighiero for kindly providing the PEP data from the deep GOODS South field. PP acknowledges the Nederlandse Organisatie voor Wetenschappelijk Onderzoek (NWO) for a PhD fellowship. MH and CW are supported by the Akademie der Wissenschaften und der Künste Nordrhein-Westfalen and by Deutsches Zentrum für Luft- und Raumfahrt (DLR). The *Herschel* spacecraft was designed, built, tested, and launched under a contract to ESA managed by the *Herschel/Planck* Project team by an industrial consortium under the overall responsibility of the prime contractor Thales Alenia Space (Cannes), and including Astrium (Friedrichshafen) responsible for the payload module and for system testing at spacecraft level, Thales Alenia Space (Turin) responsible for the service module, and Astrium (Toulouse) responsible for the telescope, with in excess of a hundred subcontractors. PACS has been developed by a consortium of institutes led by MPE (Germany) and including UVIE (Austria); KU Leuven, CSL, IMEC (Belgium); CEA, LAM (France); MPIA (Germany); INAF-IFSI/OAA/OAP/OAT, LENS, SISSA (Italy); IAC (Spain). This development has been supported by the funding agencies BMVIT (Austria), ESA-PRODEX (Belgium), CEA/CNES (France), DLR (Germany), ASI/INAF (Italy), and CICYT/MCYT (Spain). SPIRE has been developed by a consortium of institutes led by Cardiff University (UK) and including Univ. Lethbridge (Canada); NAOC (China); CEA, LAM (France); IFSI, Univ. Padua (Italy); IAC (Spain); Stockholm Observatory (Sweden); Imperial College London, RAL, UCL-MSSL, UKATC, Univ. Sussex (UK); and Caltech, JPL, NHSC, Univ. Colorado (USA). This development has been supported by national funding agencies: CSA (Canada); NAOC (China); CEA, CNES, CNRS (France); ASI (Italy); MCINN (Spain); SNSB (Sweden); STFC, UKSA (UK); and NASA (USA). HIPE is a joint development by the *Herschel* Science Ground Segment Consortium, consisting of ESA, the NASA *Herschel* Science Center, and the HIFI, PACS and SPIRE consortia. This work is partly based on observations made with the *Spitzer* Space Telescope, which is operated by the Jet Propulsion Laboratory, California Institute of Technology under a contract with NASA. This research has made use of the NASA/IPAC Extragalactic Database (NED) which is operated by the Jet Propulsion Laboratory, California Institute of Technology, under contract with the National Aeronautics and Space Administration. This research made use of APLpy, an open-source plotting package for Python hosted at <http://aplpy.github.com>.

References

Alexander, D. M., Brandt, W. N., Smail, I., et al. 2008, *AJ*, 135, 1968
 Antonucci, R. 1993, *ARA&A*, 31, 473
 Archibald, E. N., Dunlop, J. S., Hughes, D. H., et al. 2001, *MNRAS*, 323, 417
 Balog, Z., Müller, T., Nielbock, M., et al. 2013, *Experimental Astronomy*, 38
 Barthel, P. D. 1989, *ApJ*, 336, 606
 Barthel, P., Haas, M., Leipski, C., & Wilkes, B. 2012, *ApJ*, 757, L26 (B12)
 Beelen, A., Cox, P., Benford, D. J., et al. 2006, *ApJ*, 642, 694
 Bendo, G. J., Griffin, M. J., Bock, J. J., et al. 2013, *MNRAS*, 433, 3062
 Benford, D. J., Cox, P., Omont, A., Phillips, T. G., & McMahon, R. G. 1999, *ApJ*, 518, L65
 Best, P. N., Longair, M. S., & Röttgering, H. J. A. 1996, *MNRAS*, 280, L9
 Best, P. N., Longair, M. S., & Röttgering, H. J. A. 1998, *MNRAS*, 295, 549
 Best, P. N., & Heckman, T. M. 2012, *MNRAS*, 421, 1569
 Chambers, K. C., & Charlot, S. 1990, *ApJ*, 348, L1
 Cleary, K., Lawrence, C. R., Marshall, J. A., Hao, L., & Meier, D. 2007, *ApJ*, 660, 117
 Croton, D. J., Springel, V., White, S. D. M., et al. 2006, *MNRAS*, 365, 11
 De Breuck, C., Seymour, N., Stern, D., et al. 2010, *ApJ*, 725, 36
 Dey, A., van Breugel, W., Vacca, W. D., & Antonucci, R. 1997, *ApJ*, 490, 698
 Dicken, D., Tadhunter, C., Axon, D., et al. 2010, *ApJ*, 722, 1333
 Dicken, D., Tadhunter, C., Axon, D., et al. 2012, *ApJ*, 745, 172
 Draine, B. T. 2003, *ARA&A*, 41, 241

Drouart, G., De Breuck, C., Vernet, J., et al. 2014, *A&A*, 566, A53
 Elbaz, D., Daddi, E., Le Borgne, D., et al. 2007, *A&A*, 468, 33
 Elbaz, D., Dickinson, M., Hwang, H. S., et al. 2011, *A&A*, 533, A119
 Fanaroff, B. L., & Riley, J. M. 1974, *MNRAS*, 167, 31P
 Farrah, D., Urrutia, T., Lacy, M., et al. 2012, *ApJ*, 745, 178
 Fazio, G. G., Hora, J. L., Allen, L. E., et al. 2004, *ApJS*, 154, 10
 Griffin, M. J., Abergel, A., Abreu, A., et al. 2010, *A&A*, 518, L3
 Gültekin, K., Richstone, D. O., Gebhardt, K., et al. 2009, *ApJ*, 698, 198
 Haas, M., Müller, S. A. H., Bertoldi, F., et al. 2004, *A&A*, 424, 531
 Haas, M., Chini, R., Müller, S. A. H., Bertoldi, F., & Albrecht, M. 2006, *A&A*, 445, 115
 Haas, M., Willner, S. P., Heymann, F., et al. 2008, *ApJ*, 688, 122
 Harrison, C. M., Alexander, D. M., Mullaney, J. R., et al. 2012, *ApJ*, 760, L15
 Heckman, T. M., Chambers, K. C., & Postman, M. 1992, *ApJ*, 391, 39
 Hes, R., Barthel, P. D., & Hoekstra, H. 1995, *A&A*, 303, 8
 Hopkins, A. M., & Beacom, J. F. 2006, *ApJ*, 651, 142
 Hopkins, P. F., Cox, T. J., Kereš, D., & Hernquist, L. 2008, *ApJS*, 175, 390
 Houck, J. R., Roellig, T. L., van Cleve, J., et al. 2004, *ApJS*, 154, 18
 Hönig, S. F., Beckert, T., Ohnaka, K., & Weigelt, G. 2006, *A&A*, 452, 459
 Hönig, S. F., & Kishimoto, M. 2010, *A&A*, 523, A27
 Ivson, R. J., Smail, I., Amblard, A., et al. 2012, *MNRAS*, 425, 1320
 Kartaltepe, J. S., Dickinson, M., Alexander, D. M., et al. 2012, *ApJ*, 757, 23
 Kennicutt, R. C., Jr. 1998, *ARA&A*, 36, 189
 Kirkpatrick, A., Pope, A., Alexander, D. M., et al. 2012, *ApJ*, 759, 139
 Kuraszkiewicz, J. K., Wilkes, B. J., Hooper, E. J., et al. 2003, *ApJ*, 590, 128
 Leipski, C., Haas, M., Willner, S. P., et al. 2010, *ApJ*, 717, 766
 Leipski, C., Meisenheimer, K., Walter, F., et al. 2013, *ApJ*, 772, 103
 Leipski, C., Meisenheimer, K., Walter, F., et al. 2014, *ApJ*, 785, 154
 Lutz, D., Poglitsch, A., Altieri, B., et al. 2011, *A&A*, 532, A90
 Lutz, D. 2014, *ARA&A*, 52, 373
 Magnelli, B., Lutz, D., Santini, P., et al. 2012, *A&A*, 539, A155
 Magorrian, J., Tremaine, S., Richstone, D., et al. 1998, *AJ*, 115, 2285
 Markwardt, C. B. 2009, *Astronomical Data Analysis Software and Systems XVIII*, 411, 251
 McCarthy, P. J. 1993, *ARA&A*, 31, 639
 McLure, R. J., Jarvis, M. J., Targett, T. A., Dunlop, J. S., & Best, P. N. 2006, *MNRAS*, 368, 1395
 Meisenheimer, K., Haas, M., Müller, S. A. H., et al. 2001, *A&A*, 372, 719
 Michałowski, M. J., Dunlop, J. S., Cirasuolo, M., et al. 2012, *A&A*, 541, A85
 Miley, G., & De Breuck, C. 2008, *A&A Rev.*, 15, 67
 Mor, R., & Netzer, H. 2012, *MNRAS*, 420, 526
 Mullaney, J. R., Pannella, M., Daddi, E., et al. 2012, *MNRAS*, 419, 95
 Nenkova, M., Ivezić, Z., & Elitzur, M. 2002, *ApJ*, 570, L9
 Netzer, H., Lutz, D., Schweitzer, M., et al. 2007, *ApJ*, 666, 806
 Nguyen, H. T., Schulz, B., Levenson, L., et al. 2010, *A&A*, 518, L5
 O'Dea, C. P. 1998, *PASP*, 110, 493
 Ogle, P., Whysong, D., & Antonucci, R. 2006, *ApJ*, 647, 161
 Ott, S. 2010, *Astronomical Data Analysis Software and Systems XIX*, 434, 139
 Page, M. J., Symeonidis, M., Vieira, J. D., et al. 2012, *Nature*, 485, 213
 Pascale, E., Auld, R., Dariush, A., et al. 2011, *MNRAS*, 415, 911
 Pilbratt, G. L., Riedinger, J. R., Passvogel, T., et al. 2010, *A&A*, 518, L1
 Poglitsch, A., Waelkens, C., Geis, N., et al. 2010, *A&A*, 518, L2
 Popesso, P., Magnelli, B., Buttiglione, S., et al. 2012, *arXiv:1211.4257*
 Ramos Almeida, C., Levenson, N. A., Rodríguez Espinosa, J. M., et al. 2009, *ApJ*, 702, 1127
 Rawlings, J. I., Seymour, N., Page, M. J., et al. 2013, *MNRAS*, 429, 744
 Reuland, M., Röttgering, H., van Breugel, W., & De Breuck, C. 2004, *MNRAS*, 353, 377
 Rieke, G. H., Young, E. T., Engelbracht, C. W., et al. 2004, *ApJS*, 154, 25
 Rocca-Volmerange, B., Drouart, G., De Breuck, C., et al. 2013, *MNRAS*, 429, 2780
 Rodighiero, G., Cimatti, A., Gruppioni, C., et al. 2010, *A&A*, 518, L25
 Rodighiero, G., Daddi, E., Baronchelli, I., et al. 2011, *ApJ*, 739, L40
 Rosario, D. J., Santini, P., Lutz, D., et al. 2012, *A&A*, 545, A45
 Rosario, D. J., Santini, P., Lutz, D., et al. 2013, *ApJ*, 771, 63
 Rowan-Robinson, M. 1995, *MNRAS*, 272, 737
 Salpeter, E. E. 1955, *ApJ*, 121, 161
 Santini, P., Maiolino, R., Magnelli, B., et al. 2010, *A&A*, 518, L154
 Santini, P., Rosario, D. J., Shao, L., et al. 2012, *A&A*, 540, A109
 Savage, R. S., & Oliver, S. 2007, *ApJ*, 661, 1339
 Scharfmann, M., Meisenheimer, K., Camenzind, M., et al. 2008, *A&A*, 482, 67
 Schweitzer, M., Lutz, D., Sturm, E., et al. 2006, *ApJ*, 649, 79
 Seymour, N., Stern, D., De Breuck, C., et al. 2007, *ApJS*, 171, 353
 Seymour, N., Symeonidis, M., Page, M. J., et al. 2011, *MNRAS*, 413, 1777
 Seymour, N., Altieri, B., De Breuck, C., et al. 2012, *ApJ*, 755, 146
 Shao, L., Lutz, D., Nordon, R., et al. 2010, *A&A*, 518, L26
 Siebenmorgen, R., Freudling, W., Krügel, E., & Haas, M. 2004, *A&A*, 421, 129
 Silk, J. 2013, *ApJ*, 772, 112
 Spinrad, H., Marr, J., Aguilar, L., & Djorgovski, S. 1985, *PASP*, 97, 932
 Swinbank, A. M., Simpson, J. M., Smail, I., et al. 2014, *MNRAS*, 438, 1267
 Tadhunter, C., Holt, J., González Delgado, R., et al. 2011, *MNRAS*, 412, 960
 Tadhunter, C., Dicken, D., Morganti, R., et al. 2014, *MNRAS*, 445, L51
 Tremaine, S., Gebhardt, K., Bender, R., et al. 2002, *ApJ*, 574, 740
 Urry, C. M., & Padovani, P. 1995, *PASP*, 107, 803
 van Bemmel, I. M., Barthel, P. D., & Yun, M. S. 1998, *A&A*, 334, 799
 van Breugel, W. J. M., Stanford, S. A., Spinrad, H., Stern, D., & Graham, J. R. 1998, *ApJ*, 502, 614
 Venemans, B. P., Röttgering, H. J. A., Miley, G. K., et al. 2007, *A&A*, 461, 823
 Villar-Martín, M., Fosbury, R. A. E., Binette, L., Tadhunter, C. N., & Rocca-Volmerange, B. 1999, *A&A*, 351, 47
 Werner, M. W., Roellig, T. L., Low, F. J., et al. 2004, *ApJS*, 154, 1
 Wilkes, B. J., Kuraszkiewicz, J., Haas, M., et al. 2013, *ApJ*, 773, 15
 Willott, C. J., Rawlings, S., Archibald, E. N., & Dunlop, J. S. 2002, *MNRAS*, 331, 435
 Wylezalek, D., Galametz, A., Stern, D., et al. 2013, *ApJ*, 769, 79

Table 1. Summary of selected properties of the high- z 3CR sample studied in this work.

Name (1)	Type (2)	z (3)	RA (J2000) (4)	Dec (J2000) (5)	$\log(L_{178\text{MHz}} \text{ (W Hz}^{-1}\text{)})$ (6)	PACS OBSIDs (7)	SPIRE OBSIDs (8)
3C 002	QSR	1.04	00:06:22.58	-00:04:24.69	29.0	1342221796/1342221797	1342212374
3C 009	QSR	2.01	00:20:25.21	+15:40:54.59	29.8	1342222444/1342222445	1342213198
3C 013	RG	1.35	00:34:14.55	+39:24:16.65	29.2	1342223179/1342223180	1342213491
3C 014	QSR	1.47	00:36:06.44	+18:37:59.23	29.2	1342222429/1342222428	1342213196
3C 036	RG	1.30	01:17:59.48	+45:36:21.75	29.0	1342223508/1342223509	1342203613
3C 043	QSR	1.47	01:29:59.80	+23:38:20.28	29.2	1342223506/1342223507	1342213488
3C 065 ^a	RG	1.18	02:23:43.19	+40:00:52.45	29.1	1342238005/1342238006	1342239821
3C 068.1	QSR	1.24	02:32:28.87	+34:23:46.79	29.1	1342223870/1342223871	1342226628
3C 068.2	RG	1.58	02:34:23.85	+31:34:17.46	29.2	1342223866/1342223867	1342224971
3C 119	RG	1.02	04:32:36.50	+41:38:28.44	29.0	1342227975/1342227976	1342216924
3C 124	RG	1.08	04:41:59.10	+01:21:01.91	28.9	1342226718/1342226719	1342216939
3C 173	RG	1.03	07:02:20.58	+37:57:23.50	28.7	1342219418/1342219419	1342206177
3C 181	QSR	1.38	07:28:10.30	+14:37:36.24	29.3	1342220573/1342220574	1342204852
3C 186	QSR	1.06	07:44:17.45	+37:53:17.15	29.0	1342220127/1342220128	1342206178
3C 190	QSR	1.20	08:01:33.55	+14:14:42.94	29.1	1342205262/1342205263	1342205052
3C 191	QSR	1.96	08:04:47.97	+10:15:23.69	29.6	1342220655/1342220656	1342205072
3C 194	RG	1.18	08:10:03.61	+42:28:04.31	28.9	1342220123/1342220124	1342206180
3C 204	QSR	1.11	08:37:44.95	+65:13:34.92	28.9	1342220115/1342220116	1342206190
3C 205	QSR	1.53	08:39:06.45	+57:54:17.12	29.3	1342220117/1342220118	1342206188
3C 208.0	QSR	1.11	08:53:08.60	+13:52:54.98	29.1	1342220790/1342220791	1342206221
3C 208.1	RG	1.02	08:54:39.28	+14:05:52.56	28.7	1342220788/1342220789	1342206220
3C 210	RG	1.17	08:58:09.96	+27:50:51.57	28.9	1342220797/1342220796	1342230768
3C 212	QSR	1.05	08:58:41.49	+14:09:43.97	29.0	1342220786/1342220787	1342206219
3C 220.2	QSR	1.16	09:30:33.47	+36:01:24.17	28.8	1342220798/1342220799	1342222125
3C 222	RG	1.34	09:36:32.01	+04:22:10.30	29.1	1342221142/1342221143	1342210521
3C 225A	RG	1.56	09:42:08.48	+13:51:54.23	29.1	1342221258/1342221259	1342210518
3C 230	RG	1.49	09:51:58.82	-00:01:27.23	29.5	1342221136/1342221137	1342210520
3C 238	RG	1.40	10:11:00.37	+06:24:39.72	29.3	1342221144/1342221145	1342210519
3C 239 ^a	RG	1.78	10:11:45.41	+46:28:19.75	29.5	1342231241/1342231242	1342230739
3C 241	RG	1.62	10:21:54.52	+21:59:30.71	29.3	1342221152/1342221153	1342198253
3C 245	QSR	1.03	10:42:44.60	+12:03:31.26	28.9	1342221264/1342221265	1342210516
3C 249	RG	1.55	11:02:03.84	-01:16:17.39	29.5	1342221853/1342221854	1342198569
3C 250	RG	1.26	11:08:52.12	+25:00:54.61	29.1	1342221154/1342221155	1342210509
3C 252	RG	1.10	11:11:32.99	+35:40:41.64	28.9	1342221160/1342221161	1342210508
3C 255	RG	1.36	11:19:25.23	-03:02:51.50	29.2	1342221851/1342221852	1342210515
3C 256	RG	1.82	11:20:43.02	+23:27:55.22	29.4	1342221262/1342221263	1342210510
3C 257	RG	2.47	11:23:09.17	+05:30:19.47	29.7	1342221966/1342221967	1342210514
3C 266 ^a	RG	1.27	11:45:43.36	+49:46:08.24	29.1	1342222695/1342222696	1342222663
3C 267	RG	1.14	11:49:56.56	+12:47:19.07	29.1	1342222448/1342222449	1342200236
3C 268.4	QSR	1.40	12:09:13.61	+43:39:20.96	29.1	1342221162/1342221163	1342210501
3C 270.1	QSR	1.52	12:20:33.87	+33:43:12.05	29.3	1342221952/1342221953	1342200238
3C 280.1	QSR	1.66	13:00:33.30	+40:09:07.72	29.3	1342212393/1342212394	1342210498
3C 294 ^a	RG	1.78	14:06:53.20	+34:11:21.10	29.4	1342211098/1342211099	1342206200
3C 297	RG	1.41	14:17:23.99	-04:00:47.54	29.1	1342223834/1342223835	1342203577
3C 298	QSR	1.44	14:19:08.18	+06:28:34.80	29.8	1342223664/1342223665	1342213464
3C 305.1	RG	1.13	14:47:09.56	+76:56:21.80	29.0	1342220952/1342220953	1342206193
3C 318	QSR	1.57	15:20:05.44	+20:16:05.76	29.3	1342223844/1342223845	1342204107
3C 322	RG	1.68	15:35:01.23	+55:36:52.87	29.3	1342199131/1342199132	1342206196
3C 324	RG	1.21	15:49:48.89	+21:25:38.06	29.2	1342202562/1342202563	1342213461

Table 1. continued.

Name (1)	Type (2)	z (3)	RA (J2000) (4)	Dec (J2000) (5)	$\log(L_{178\text{MHz}} \text{ (W Hz}^{-1}\text{)})$ (6)	PACS OBSIDs (7)	SPIRE OBSIDs (8)
3C 325	QSR	1.13	15:49:58.42	+62:41:21.66	29.1	1342219034/1342219035	1342206195
3C 326.1	RG	1.83	15:56:10.06	+20:04:20.44	29.3	1342224482/1342224483	1342213462
3C 356	RG	1.08	17:24:19.04	+50:57:40.14	28.9	1342219036/1342219037	1342206197
3C 368	RG	1.13	18:05:06.45	+11:01:35.06	29.0	1342216599/1342216600	1342216954
3C 418	QSR	1.69	20:38:37.03	+51:19:12.66	29.4	1342219032/1342219033	1342210542
3C 432	QSR	1.80	21:22:46.32	+17:04:37.95	29.4	1342211499/1342211500	1342210541
3C 437	RG	1.48	21:47:25.10	+15:20:37.49	29.3	1342211497/1342211498	1342210540
3C 454.0	QSR	1.76	22:51:34.73	+18:48:40.12	29.4	1342210949/1342210950	1342210539
3C 454.1	RG	1.84	22:50:32.93	+71:29:19.18	29.4	1342211436/1342211437	1342212365
3C 469.1	RG	1.34	23:55:23.32	+79:55:19.60	29.1	1342221170/1342221171	1342220543
3C 470 ^a	RG	1.65	23:58:35.89	+44:04:45.55	29.3	1342237858/1342237859	1342236248
4C 13.66	RG	1.45	18:01:38.95	+13:51:23.85	29.2	1342216597/1342216598	1342216956
4C 16.49	QSR	1.30	17:34:42.61	+16:00:31.21	29.1	1342216595/1342216596	1342216955

Notes. (1) Name of object; (2) AGN type; (3) Redshift; (4) Right Ascension; (5) Declination; (6) Log of 178 MHz luminosity (in the observer frame); (7) PACS ObsID; (8) SPIRE ObsID

^(a) *Herschel* observations taken from OT1_nseymour_1 (PI: Seymour)

Table 2. *Herschel* and *Spitzer* photometry of the 3CR objects studied in this work. Photometric uncertainties are 1σ values, and upper limits are 3σ values.

Object	F _{3.6μm} (μJy)	F _{4.5μm} (μJy)	F _{5.8μm} (μJy)	F _{8.0μm} (μJy)	F _{16μm} (μJy)	F _{24μm} (μJy)	F _{70μm} (mJy)	F _{160μm} (mJy)	F _{250μm} (mJy)	F _{350μm} (mJy)	F _{500μm} (mJy)
(1)	(2)	(3)	(4)	(5)	(6)	(7)	(8)	(9)	(10)	(11)	(12)
3C 002	283±42	330±50	530±80	809±121	1550±233	2970±446	10.0±2.6	21.9±4.4	16.1±5.1	19.6±4.8	< 17.0
3C 009	884±133	1080±162	1590±239	2220±333	3330±500	3470±520	13.7±2.6	18.1±4.9	< 15.4	< 13.8	< 17.2
3C 013	133±20	133±20	147±22	283±42	375±56	2060±309	24.6±2.1	30.7±5.8	< 18.8	< 15.3	< 20.7
3C 014	1040±156	1710±257	2740±411	4150±623	7070±1061	10300±1545	20.9±2.6	21.9±6.8	20.0±6.3	< 15.4	< 19.8
3C 036	163±24	205±31	256±38	360±54	560±84	874±131	< 4.2	< 10.6	< 11.2	< 11.8	< 14.2
3C 043	193±29	270±41	356±53	445±67	1010±152	1610±242	... ^b	... ^b	< 14.1	< 17.9	< 15.8
3C 065	202±30	233±35	299±45	418±63	798±120	1700±255	< 6.7	< 12.1	< 20.8	< 18.1	< 20.2
3C 068.1	967±145	1430±215	2040±306	2780±417	3800±570	7760±1164	22.7±2.3	< 17.8	< 18.2	< 15.9	< 20.1
3C 068.2	105±16	129±19	137±21	112±17	1340±201	1170±176	27.4±2.6	39.6±5.9	42.0±7.2	38.7±7.0	29.0±7.2
3C 119	802±120	878±132	1280±192	1850±278	4820±723	8260±1239	24.9±2.2	32.6±8.9	28.9±15.4 ^a	< 56.1	< 44.1
3C 124	144±22	120±18	188±28	310±47	1840±276	3560±534	34.2±2.1	55.7±6.7	52.1±7.3	31.5±7.9	< 24.3
3C 173	163±24	172±26	197±30	227±34	374±56	710±107	6.9±1.6	< 10.2	< 11.6	< 13.0	< 16.5
3C 181	348±52	485±73	722±108	1110±167	2180±327	4260±639	12.2±2.3	< 13.6	< 20.4	< 16.5	< 21.8
3C 186	791±119	1020±153	1410±212	1960±294	3660±549	6660±999	18.9±2.6	< 18.0	< 13.7	< 17.1	< 21.0
3C 190	739±111	908±136	1290±194	1740±261	3310±497	6690±1004	46.1±2.5	72.5±4.8	74.1±6.5	54.1±4.7	< 20.9
3C 191	333±50	399±60	655±98	1010±152	2270±341	3810±572	26.4±2.7	21.9±4.9	< 18.9	< 17.1	< 18.1
3C 194	201±30	176±26	164±25	208±31	509±76	885±133	< 4.6	< 9.3	< 20.2	< 18.9	< 20.7
3C 204	917±138	1250±188	1920±288	2540±381	4730±710	7360±1104	< 6.1	< 13.5	< 17.9	< 14.5	< 18.2
3C 205	1460±219	2080±312	2920±438	4090±614	7320±1098	12800±1920	62.7±2.6	66.2±6.8	56.2±6.8	31.6±4.8	19.9±6.7 ^a
3C 208.0	660±99	803±120	1160±174	1620±243	2980±447	5870±881	< 7.4	< 16.7	< 20.5	< 21.7	< 20.3
3C 208.1	331±50	430±65	656±98	954±143	1360±204	2110±317	< 8.1	< 15.7	< 17.1	< 16.0	< 20.2
3C 210	256±38	336±50	489±73	1090±164	3410±512	4430±665	31.6±2.4	56.0±4.0	... ^b	... ^b	... ^b
3C 212	925±139	1430±215	2340±351	3400±510	6710±1007	10800±1620	16.6±2.6	< 16.7	< 38.5	< 56.0	< 39.9
3C 220.2	592±89	870±131	1330±200	2000±300	4150±623	6720±1008	26.6±2.2	22.5±5.3	< 14.1	< 14.6	< 15.7
3C 222	83±12	91±14	73±11	65±10	331±50	229±34	14.3±1.9	50.8±4.7	48.4±4.8	50.9±3.5	28.7±5.4
3C 225A	47±7	49±7	71±11	108±16	321±48	< 1070	< 7.8	< 21.4	< 21.3	< 16.3	< 22.7
3C 230	1040±156	672±101	438±66	317±48	1150±173	1560±234	11.9±2.3	< 19.8	< 40.7	< 36.1	< 34.7
3C 238	65±10	77±12	84±12	< 92	< 283	266±40	< 4.0	< 8.2	< 13.4	< 14.2	< 17.3
3C 239	96±14	111±17	130±20	142±21	651±98	1450±218	< 7.3	< 15.3	< 19.1	< 14.9	< 21.0
3C 241	92±14	101±15	116±17	161±24	389±58	591±89	7.9±1.1	< 8.2	< 15.5	< 12.5	< 17.6
3C 245	1420±213	1900±285	3350±503	5270±790	10400±1560	20400±3060	47.5±2.4	35.3±6.4	35.2±5.9	< 16.1	< 22.3
3C 249	54±8	52±8	42±6	47±7	194±29	< 516	< 3.2	< 10.7	< 11.5	< 10.4	< 14.4
3C 250	61±9	59±9	46±7	29±4	162±24	< 147	< 3.7	< 10.7	< 11.8	< 15.0	< 13.9
3C 252	225±34	382±57	787±118	1390±209	3900±585	7000±1050	21.4±2.4	< 21.3	< 17.2	< 17.4	< 23.1

Table 2. continued.

Object	F _{3.6μm} (μJy)	F _{4.5μm} (μJy)	F _{5.8μm} (μJy)	F _{8.0μm} (μJy)	F _{16μm} (μJy)	F _{24μm} (μJy)	F _{70μm} (mJy)	F _{160μm} (mJy)	F _{250μm} (mJy)	F _{350μm} (mJy)	F _{500μm} (mJy)
(1)	(2)	(3)	(4)	(5)	(6)	(7)	(8)	(9)	(10)	(11)	(12)
3C 255	85±13	86±13	57±9	22±3	< 116	< 241	< 3.2	< 8.4	< 14.5	< 17.0	< 19.1
3C 256	34±5	37±6	43±7	75±11	743±111	1900±285	17.8±2.3	31.9±5.3	28.2±6.9	< 19.1	< 21.6
3C 257	85±13	111±17	194±29	322±48	...	1360±204	8.1±1.0	15.6±2.5	33.1±4.7	31.8±5.5	32.3±8.6
3C 266	68±10	73±11	45±7	102±15	370±56	980±147	7.6±2.4	29.4±4.1	19.5±5.6	< 15.9	< 18.9
3C 267	153±23	218±33	414±62	739±111	2370±356	3730±560	15.3±2.3	< 12.7	< 16.8	< 14.1	< 19.1
3C 268.4	1060±159	1560±234	2220±333	3330±500	7580±1137	11600±1740	30.3±2.1	< 17.0	< 18.7	< 18.2	< 24.3
3C 270.1	606±91	944±142	1430±214	2260±339	3910±587	5470±821	30.0±2.2	38.9±4.7	27.9±5.5	< 17.5	< 19.6
3C 280.1	378±57	512±77	777±116	1170±176	1680±252	2160±324	< 5.0	< 9.4	< 17.0	< 13.4	< 17.2
3C 294	< 93	< 103	68±10	67±10	...	348±52	< 6.6	< 22.1	< 16.6	< 14.5	< 21.9
3C 297	119±18	126±19	122±18	121±18	< 288	432±65	12.6±1.2	15.4±2.4	24.5±4.3	< 13.8	< 17.2
3C 298	1600±240	2390±359	3710±556	5510±827	9160±1374	12600±1890	78.7±2.4	96.8±4.3	96.0±6.9	51.5±5.9	24.1±6.7
3C 305.1	181±27	282±42	495±74	972±146	2410±362	2490±374	24.0±2.3	40.4±4.3	34.9±6.0	< 18.1	< 18.9
3C 318	343±51	427±64	571±86	806±121	1960±294	3400±510	18.3±2.3	43.8±5.9	42.9±6.1	... ^b	... ^b
3C 322	128±19	135±20	94±14	120±18	411±62	804±121	< 5.0	< 11.0	< 19.0	< 17.5	< 21.9
3C 324	165±25	160±24	178±27	450±68	2580±387	2820±423	23.5±2.3	31.7±5.6	21.0±6.2	< 18.2	< 21.4
3C 325	472±71	565±85	708±106	1200±180	1990±299	3030±455	< 7.6	< 18.4	< 15.4	< 16.1	< 18.3
3C 326.1	29±4	34±5	26±4	72±11	829±124	1430±215	< 6.7	< 14.5	29.8±5.9	21.0±6.9	< 20.8
3C 356	108±16	110±16	122±18	434±65	2270±341	4060±609	11.6±2.5	19.7±4.9	< 18.4	< 15.3	< 20.4
3C 368	126±19	112±17	112±17	210±32	1370±206	3250±488	29.9±2.0	61.5±4.8	44.4±7.4	23.8±6.2	< 21.3
3C 418	1130±170	1630±245	2470±371	3900±585	6680±1002	13600±2040	95.1±2.6	200.1±16.1	173.8±40.0	259.2±43.7	387.4±28.6
3C 432	420±63	526±79	857±129	1490±224	2710±407	3940±591	< 7.3	< 13.8	34.7±5.1	25.2±5.1	30.7±5.8
3C 437	82±12	85±13	97±15	80±12	384±58	941±141	< 6.4	< 18.4	< 17.0	< 14.3	< 18.9
3C 454.0	339±51	481±72	811±122	1220±183	2490±374	4150±623	15.7±2.2	39.5±5.2	31.0±5.6	35.3±5.2	28.0±7.2
3C 454.1	77±12	76±11	112±17	135±20	612±92	1500±225	13.7±2.5	37.0±4.7	50.2±8.7	26.7±10.4 ^a	< 50.0
3C 469.1	160±24	244±37	509±76	1090±164	3270±491	1970±296	10.9±2.3	24.3±4.6	< 20.9	< 19.1	< 21.8
3C 470	50±7	75±11	72±11	266±40	1510±227	2650±398	16.0±2.7	29.3±5.1	48.0±6.5	36.3±5.2	< 21.5
4C 13.66	24±4	24±4	21±3	18±3	< 260	276±41	< 5.5	< 13.4	< 15.6	< 13.9	< 17.9
4C 16.49	329±49	420±63	573±86	743±111	1070±161	1830±275	< 5.0	< 17.3	< 18.5	< 18.7	< 23.2

Notes.^(a) Less than 3σ detection entering our SED fitting routine.^(b) Photometric measurement hindered by the presence of a nearby source.

Table 4. Physical parameters estimated from the SED fitting.

Object	L_{AGN} ($10^{12} L_{\odot}$)	L_{SF} ($10^{12} L_{\odot}$)	SFR ($10^2 M_{\odot} \text{ yr}^{-1}$)	M_d ($10^8 M_{\odot}$)	T_d (K)
(1)	(2)	(3)	(4)	(5)	(6)
Objects detected in at least three <i>Herschel</i> bands					
3C 002	$2.1^{+0.1}_{-0.2}$	$0.6^{+0.2}_{-0.1}$	$1.1^{+0.4}_{-0.2}$	$1.1^{+0.7}_{-0.7}$	$31.6^{+9.2}_{-3.1}$
3C 014	$16.1^{+0.5}_{-0.5}$	$1.3^{+0.3}_{-0.2}$	$2.3^{+0.5}_{-0.3}$	$0.9^{+1.1}_{-0.4}$	$37.5^{+5.1}_{-5.7}$
3C 068.2	$6.6^{+0.4}_{-0.3}$	$2.1^{+0.2}_{-0.3}$	$3.7^{+0.4}_{-0.4}$	$7.0^{+2.2}_{-2.0}$	$28.5^{+2.3}_{-1.7}$
3C 119 ^a	$4.4^{+0.3}_{-0.4}$	$0.9^{+0.2}_{-0.1}$	$1.5^{+0.4}_{-0.3}$	$0.7^{+2.8}_{-0.3}$	$37.6^{+5.4}_{-9.7}$
3C 124	$3.7^{+0.1}_{-0.1}$	$1.5^{+0.1}_{-0.1}$	$2.7^{+0.2}_{-0.3}$	$2.6^{+0.6}_{-0.6}$	$31.9^{+2.2}_{-1.3}$
3C 190	$9.0^{+0.4}_{-0.4}$	$2.7^{+0.1}_{-0.1}$	$4.7^{+0.2}_{-0.1}$	$4.9^{+0.2}_{-0.5}$	$31.7^{+0.6}_{-0.3}$
3C 205	$27.9^{+0.8}_{-0.8}$	$4.1^{+0.3}_{-0.3}$	$7.0^{+0.5}_{-0.6}$	$1.8^{+0.3}_{-0.2}$	$40.7^{+1.1}_{-1.8}$
3C 222	$1.5^{+0.1}_{-0.1}$	$2.5^{+0.1}_{-0.1}$	$4.3^{+0.2}_{-0.2}$	$5.4^{+0.7}_{-0.7}$	$30.6^{+1.0}_{-0.8}$
3C 245	$11.2^{+0.5}_{-0.4}$	$0.8^{+0.1}_{-0.1}$	$1.4^{+0.2}_{-0.2}$	$2.4^{+1.0}_{-0.8}$	$28.8^{+3.4}_{-2.0}$
3C 256	$6.9^{+0.5}_{-0.5}$	$2.6^{+0.4}_{-0.2}$	$4.5^{+0.7}_{-0.4}$	$0.9^{+0.7}_{-0.2}$	$43.0^{+1.4}_{-4.3}$
3C 257 ^{a d}	$8.0^{+0.4}_{-0.6}$	$5.4^{+0.3}_{-0.3}$	$9.2^{+0.6}_{-0.5}$	$3.4^{+0.4}_{-0.4}$	$38.2^{+1.1}_{-0.9}$
3C 266	$1.0^{+0.2}_{-0.3}$	$1.5^{+0.2}_{-0.2}$	$2.7^{+0.3}_{-0.3}$	$0.4^{+0.1}_{-0.1}$	$44.2^{+0.7}_{-1.9}$
3C 270.1	$12.7^{+0.5}_{-0.4}$	$2.3^{+0.4}_{-0.2}$	$3.9^{+0.6}_{-0.4}$	$0.8^{+0.2}_{-0.2}$	$43.5^{+1.2}_{-2.8}$
3C 297	$2.2^{+0.1}_{-0.2}$	$0.9^{+0.1}_{-0.1}$	$1.6^{+0.2}_{-0.2}$	$6.5^{+3.7}_{-2.2}$	$24.9^{+1.7}_{-1.8}$
3C 298 ^d	$29.2^{+0.8}_{-0.8}$	$5.4^{+0.2}_{-0.2}$	$9.3^{+0.4}_{-0.3}$	$3.8^{+0.3}_{-0.4}$	$37.5^{+0.8}_{-0.8}$
3C 305.1 ^a	$3.4^{+0.2}_{-0.3}$	$1.3^{+0.3}_{-0.1}$	$2.2^{+0.4}_{-0.2}$	$1.4^{+0.6}_{-0.7}$	$34.7^{+6.7}_{-2.6}$
3C 318	$7.6^{+0.4}_{-0.4}$	$3.4^{+0.4}_{-0.3}$	$5.8^{+0.6}_{-0.5}$	$1.7^{+0.6}_{-0.4}$	$39.6^{+2.7}_{-1.9}$
3C 324	$3.6^{+0.2}_{-0.2}$	$1.0^{+0.2}_{-0.2}$	$1.8^{+0.4}_{-0.3}$	$0.5^{+0.5}_{-0.1}$	$39.6^{+3.3}_{-4.4}$
3C 368 ^d	$3.3^{+0.2}_{-0.2}$	$2.0^{+0.2}_{-0.2}$	$3.5^{+0.4}_{-0.3}$	$1.4^{+0.4}_{-0.3}$	$37.3^{+2.6}_{-1.6}$
3C 432 ^d	$9.3^{+0.7}_{-0.4}$	$2.4^{+0.2}_{-0.2}$	$4.2^{+0.4}_{-0.4}$	$6.4^{+1.3}_{-1.4}$	$29.8^{+1.1}_{-1.6}$
3C 454.0	$10.5^{+0.4}_{-0.5}$	$3.6^{+0.3}_{-0.2}$	$6.2^{+0.6}_{-0.4}$	$2.3^{+0.6}_{-0.5}$	$38.3^{+2.0}_{-2.0}$
3C 454.1	$5.2^{+0.5}_{-0.7}$	$4.4^{+0.2}_{-0.4}$	$7.5^{+0.4}_{-0.7}$	$2.4^{+0.7}_{-0.7}$	$39.3^{+2.2}_{-2.0}$
3C 470 ^d	$5.8^{+0.3}_{-0.3}$	$3.0^{+0.2}_{-0.2}$	$5.1^{+0.4}_{-0.3}$	$4.5^{+0.5}_{-0.7}$	$32.8^{+1.1}_{-1.0}$
Objects detected in fewer than three <i>Herschel</i> bands					
3C 009	17.1	< 1.8	< 3.1		
3C 013	4.0	< 1.2	< 2.0		
3C 036 ^{a b}	< 1.2	< 0.5	< 0.9		
3C 043	2.8	< 1.2	< 2.0		
3C 065 ^{a b}	< 1.4	< 0.6	< 1.0		
3C 068.1 ^c	8.6	< 0.7	< 1.1		
3C 173 ^b	0.4	< 0.3	< 0.5		
3C 181 ^c	5.2	< 0.8	< 1.5		
3C 186 ^c	4.7	< 0.5	< 0.8		
3C 191	17.0	< 1.7	< 3.0		
3C 194 ^b	< 0.7	< 0.6	< 0.9		
3C 204 ^c	< 4.8	< 0.5	< 0.9		
3C 208.0	< 3.6	< 0.6	< 1.0		
3C 208.1 ^a	< 1.6	< 0.4	< 0.7		
3C 210 ^a	5.2	< 1.9	< 3.3		
3C 212	6.2	< 0.8	< 1.3		
3C 220.2	6.3	< 0.7	< 1.2		
3C 225A ^b	< 1.5	< 1.8	< 3.1		
3C 230	3.1	< 1.9	< 3.3		
3C 238 ^b	< 0.7	< 0.5	< 0.9		
3C 239 ^b	< 3.0	< 1.7	< 2.9		
3C 241 ^b	2.1	< 0.8	< 1.4		
3C 249 ^b	< 0.9	< 0.8	< 1.5		

Table 4. continued.

Object	L_{AGN} ($10^{12} L_{\odot}$)	L_{SF} ($10^{12} L_{\odot}$)	SFR ($10^2 M_{\odot} \text{ yr}^{-1}$)	M_d ($10^8 M_{\odot}$)	T_d (K)
(1)	(2)	(3)	(4)	(5)	(6)
3C 250	< 0.6	< 0.5	< 0.9		
3C 252 ^a	4.5	< 0.6	< 1.0		
3C 255 ^b	< 0.5	< 0.5	< 0.9		
3C 267 ^a	3.1	< 0.4	< 0.7		
3C 268.4	16.2	< 0.8	< 1.4		
3C 280.1 ^c	< 5.4	< 1.1	< 1.9		
3C 294 ^b	< 2.3	< 1.7	< 2.9		
3C 322	< 1.5	< 1.3	< 2.2		
3C 325	< 2.5	< 0.7	< 1.2		
3C 326.1	< 3.7	< 3.0	< 5.2		
3C 356	1.9	< 0.8	< 1.3		
3C 437 ^b	< 1.6	< 1.2	< 2.1		
3C 469.1 ^a	3.3	< 1.3	< 2.2		
4C 13.66	< 1.0	< 0.8	< 1.4		
4C 16.49 ^c	< 2.4	< 0.9	< 1.5		

Notes. (1) Name of object; (2) IR luminosity (integrated between $1 \mu\text{m}$ and $1000 \mu\text{m}$) of the AGN powered dust emission, i.e. torus component and sum of torus and hot dust components for RGs and QSRs, respectively; (3) IR luminosity (integrated between $8 \mu\text{m}$ and $1000 \mu\text{m}$) of the modified blackbody component ($\beta = 1.6$) presumably powered by star formation activity in the AGN host galaxy; (4) star formation rate determined from the IR luminosity in (3), using the calibration derived in Kennicutt (1998); (5) mass of the modified blackbody component; (6) temperature of the modified blackbody component.

^(a) For this radio galaxy, a blackbody component (1300 K) was included in the SED fitting.

^(b) This object was included in the stacking of non-detected radio galaxies.

^(c) This object was included in the stacking of non-detected quasars.

^(d) The emissivity index of the cold dust component, β , was estimated for this object.

Appendix A: UV/visible SEDs of quasars

The emission from powerful quasars at UV/visible wavelengths comes predominantly from the hot accretion disk. In quasar SED fitting, this component is typically represented by a power-law (PL), extended to the NIR by introducing a PL index of -2 ($F_\nu \propto \nu^{-2}$) (e.g. Leipski et al. 2013). In the current work, we do not fit the rest-frame UV/visible SEDs of quasars because it has a negligible influence on the FIR part of the SED. We demonstrate this using two objects that have good coverage in the UV/visible: 3C 454.0 and 3C 002.

Firstly, we consider 3C 454.0 (upper panels of Fig. A.1), for which we have SDSS photometry (*ugriz*) in addition to the *Spitzer* and *Herschel* photometry, and compare the results when we include/exclude the PL component. In a first attempt, we fit the data using a PL component in addition to the 1300 K blackbody, torus, and star-formation-heated cold dust components. Given the redshift of 3C 454.0, strong MgII emission at rest-frame $\sim 0.3 \mu\text{m}$, typical for optical spectra of quasars, significantly contributes to its broad-band *i* and *z* photometry. The SED fitting including the PL component was therefore performed using only the *u*, *g*, and *r* SDSS photometry. In a second attempt, we fit only data at rest-frame wavelengths longer than $2 \mu\text{m}$, excluding the PL component from the fit. As seen in Fig. A.1, the best-fit SEDs longward of $2 \mu\text{m}$ rest-frame wavelength are very similar for the two fitting approaches. The only difference is the flux normalization of the hot dust component, which turns out to be slightly lower when including the UV/visible part of the SED. Understandably, this is a result of the PL component contributing to the emission in the shorter *Spitzer* wavelengths. While the fitting procedures prefer different torus models, the luminosity of this component changes by less than 10%. Most importantly, the most relevant physical parameters for the current work: the star formation rate, and the temperature and mass of the cold dust component remain within 10%.

Secondly, we consider 3C 002 (lower panels of Fig. A.1), for which in addition to SDSS, *Spitzer* and *Herschel* photometry, we have photometry from 2MASS. We fit the full SED of this object, after discarding data points potentially contaminated by strong emission lines. Once again we reach the same results as in the case for 3C 454.0, thus we conclude that a detailed treatment of the emission in the UV/visible part of the quasars' SEDs has a negligible effect on the results inferred from the IR part of the SED. Furthermore, many 3CR quasars lack good UV/visible/NIR photometric data, making the inclusion of the PL component to the fitting procedure impossible. Consequently, the results presented in our work were obtained using the best-fit SEDs without fitting a PL to the UV/visible part of the SEDs of quasars.

Appendix B: Comments on individual objects

3C 036 - This source requires an additional hot dust component to better fit the data.

3C 043 - There is a bright nearby object dominating the emission in the PACS $160 \mu\text{m}$ band. We report no measurement in this band.

3C 065 - This source requires an additional hot dust component to better fit the data.

3C 068.2 - IRS $16 \mu\text{m}$ data point is removed from the fitting procedure.

3C 119 - Diffuse emission present in the PACS $160 \mu\text{m}$ and SPIRE maps owing to the object's low galactic latitude. This source requires an additional hot dust component to better fit the

data.

3C 208.1 - This source requires an additional hot dust component to better fit the data.

3C 210 - Bright nearby object present in SPIRE bands. Deblending is not possible. We report no measurements in the SPIRE bands. Photometry in PACS $160 \mu\text{m}$ was performed with an aperture of $6''$ radius. This source requires an additional hot dust component to better fit the data. IRAC $8 \mu\text{m}$ and IRS $16 \mu\text{m}$ data are not well fitted.

3C 222 - IRS $16 \mu\text{m}$ data point is removed from the fitting procedure.

3C 230 - The *Spitzer* photometry probably includes a star located very close to the radio galaxy. IRAC $3.6 \mu\text{m}$, IRAC $4.5 \mu\text{m}$, and IRAC $5.8 \mu\text{m}$ data points are removed from the fitting procedure.

3C 252 - This source requires an additional hot dust component to better fit the data.

3C 255 - The IRAC points are not well-fitted with the blackbody component representing emission from old stars in the host galaxy.

3C 257 - This source requires an additional hot dust component to better fit the data.

3C 267 - This source requires an additional hot dust component to better fit the data.

3C 305.1 - This source requires an additional hot dust component to better fit the data. IRAC $8 \mu\text{m}$ and IRS $16 \mu\text{m}$ data are not well fitted.

3C 318 - Bright nearby object present in PACS and SPIRE bands. Deblending is not possible for SPIRE $350 \mu\text{m}$ and SPIRE $500 \mu\text{m}$. We report no measurement in these two bands.

3C 324 - IRAC $8 \mu\text{m}$ and IRS $16 \mu\text{m}$ data are not well fitted.

3C 418 - The only flat-spectrum-core-dominated object within the high-*z* 3CR sample; completely synchrotron dominated. We do not include this source in the analysis.

3C 454.1 - Diffuse emission present in SPIRE maps.

3C 469.1 - The PACS $160 \mu\text{m}$ flux density might be slightly contaminated by a nearby object. This source requires an additional hot dust component to better fit the data. IRAC $8 \mu\text{m}$ and IRS $16 \mu\text{m}$ data are not well fitted.

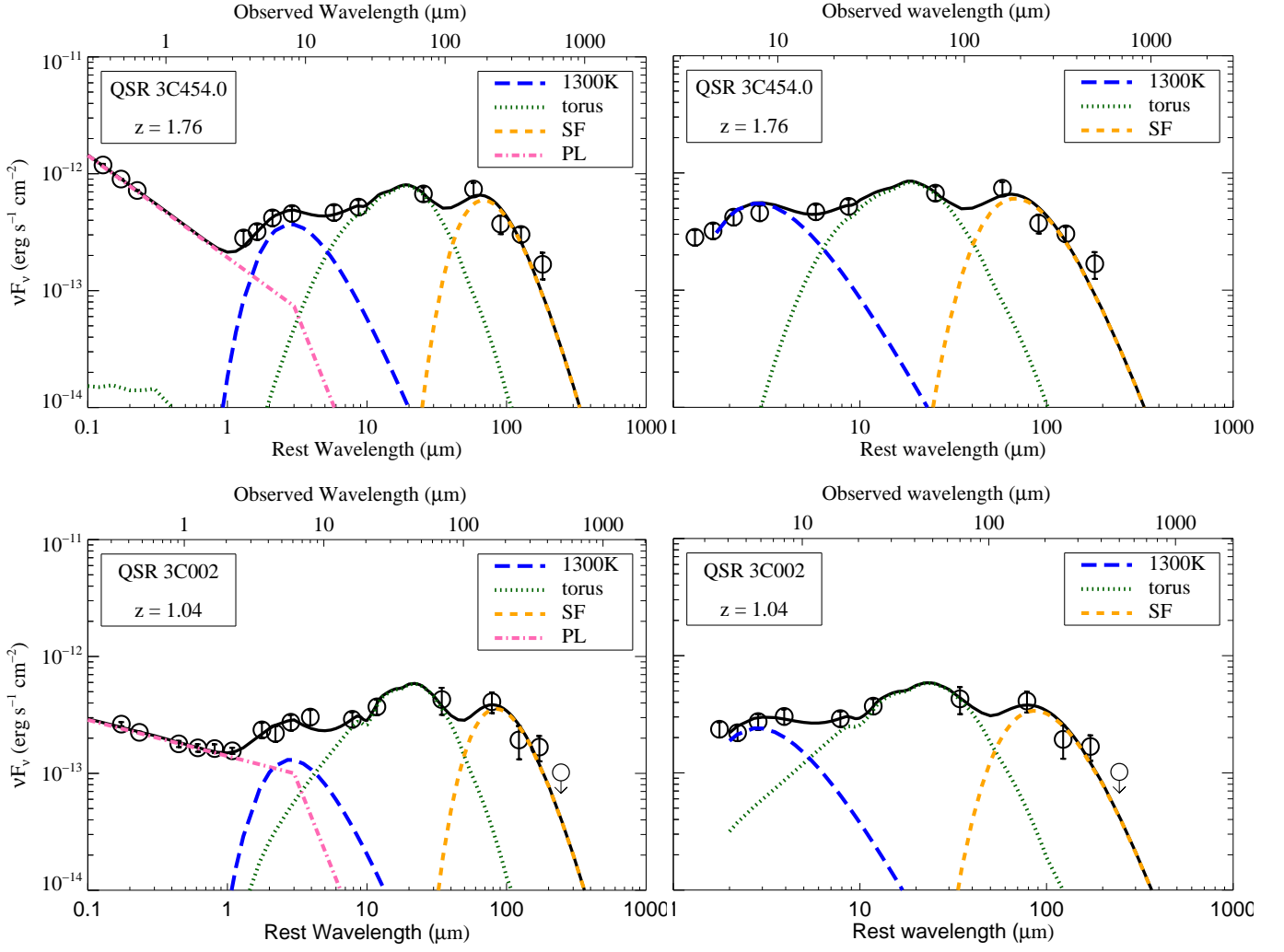


Fig. A.1. Spectral energy distributions of two quasars with good visible/UV detections. Left panels include a power-law component (dash-dotted pink) representing the emission from the hot accretion disk. Right panels exclude that component, and show the components considered when fitting the quasars in this work. Other individual components as described in Fig. 2.

Appendix C: Best-fit SEDs of objects detected in at least three *Herschel* bands

Appendix D: Best-fit SEDs of objects detected in fewer than three *Herschel* bands

Appendix E: Postage stamps

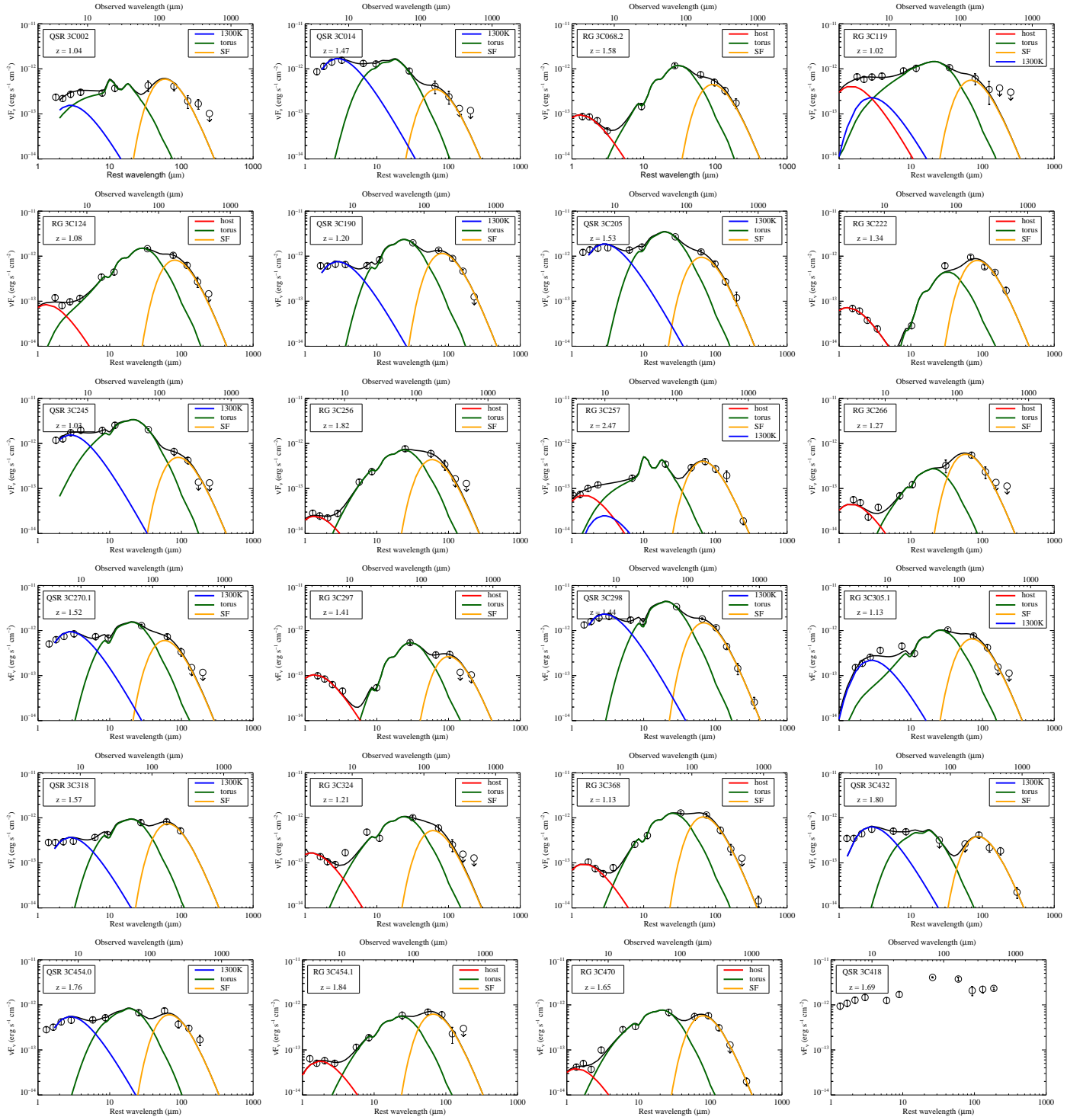


Fig. C.1. Spectral energy distributions of the 24 objects detected in at least three *Herschel* bands. Individual components as described in Fig. 2. 3C 418 was not included in the analysis, as discussed in Sect. 3.3

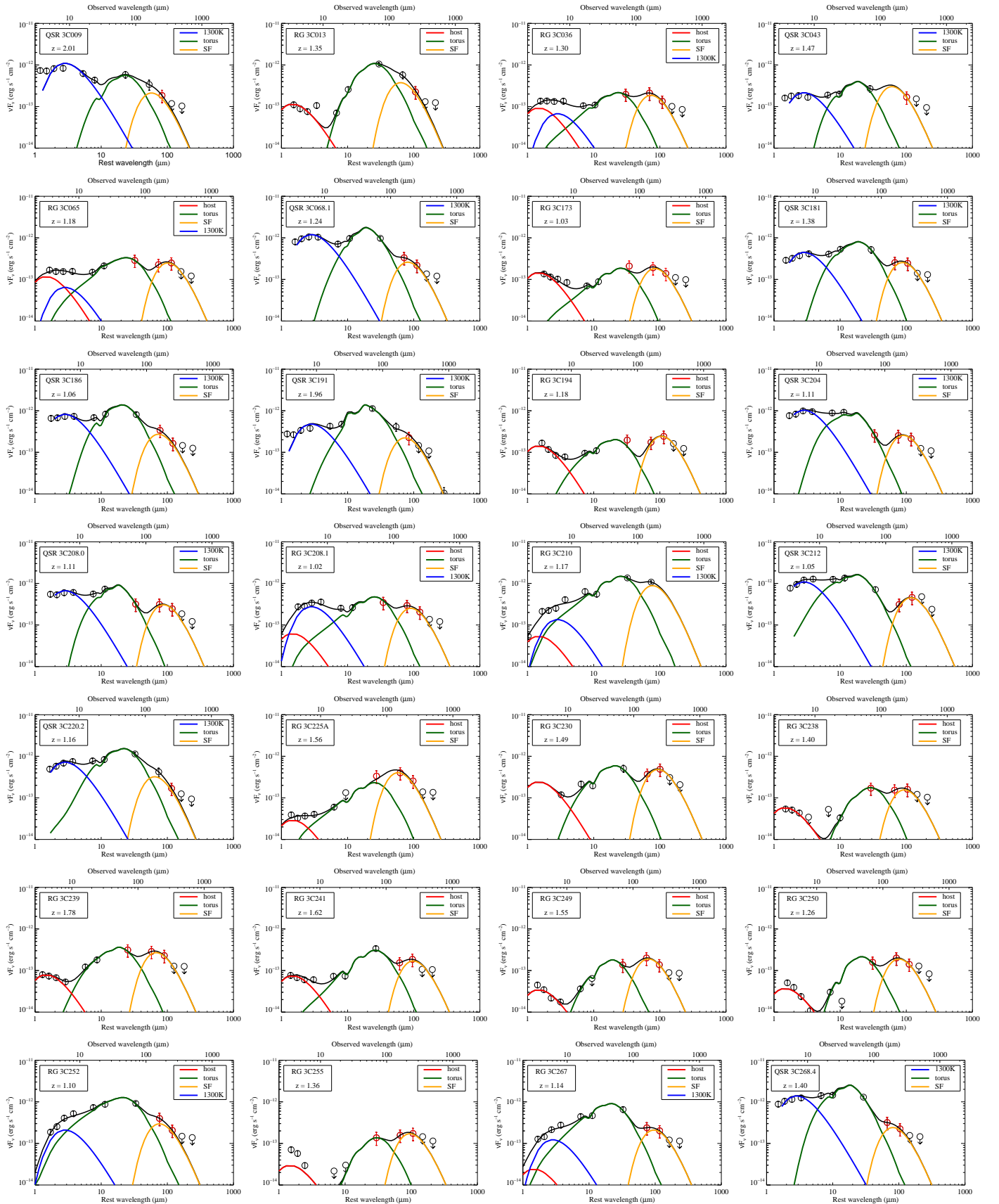


Fig. D.1. Spectral energy distributions of the objects detected in fewer than three *Herschel* bands. Individual components as described in Fig. 2. Red circles denote 3σ upper limits taken to be tentative detections when calculating upper limits of physical parameters, as explained in Sect. 3.

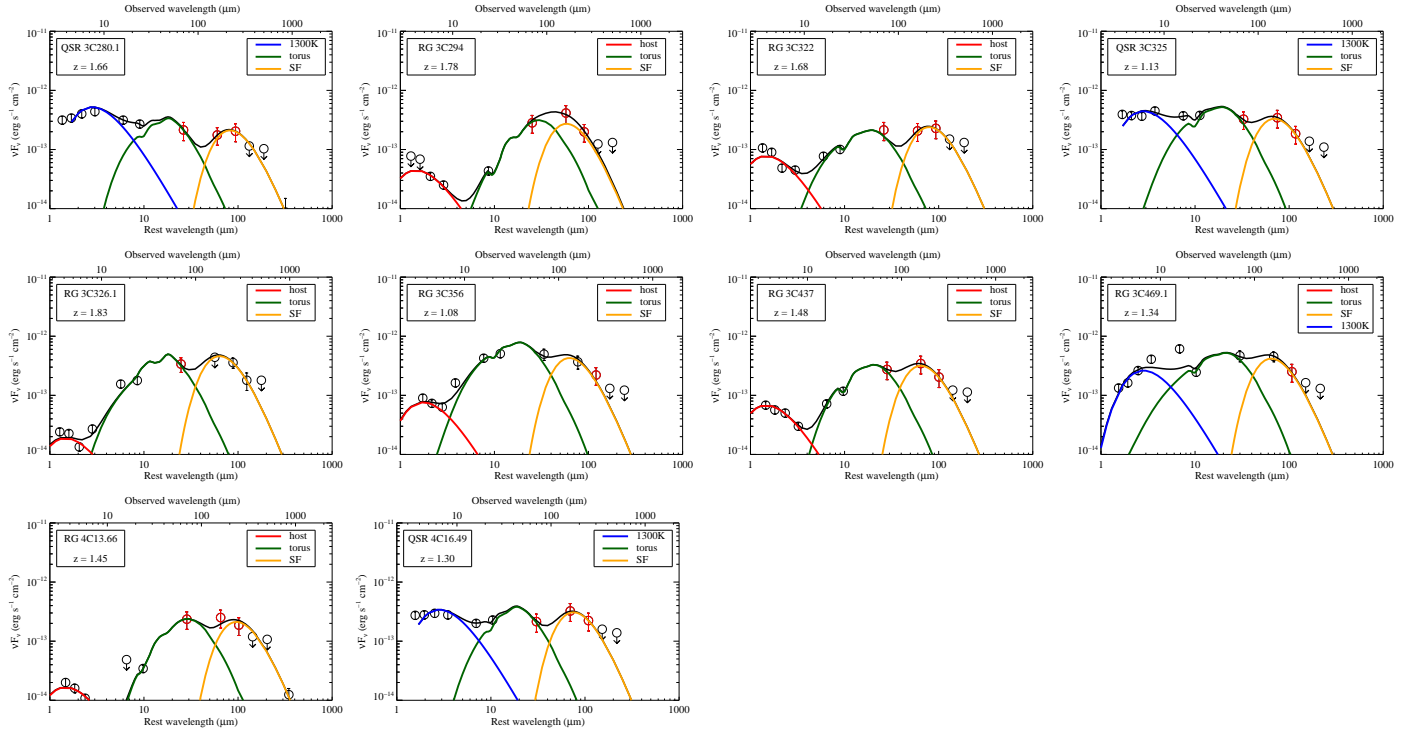


Fig. D.1. Continued.

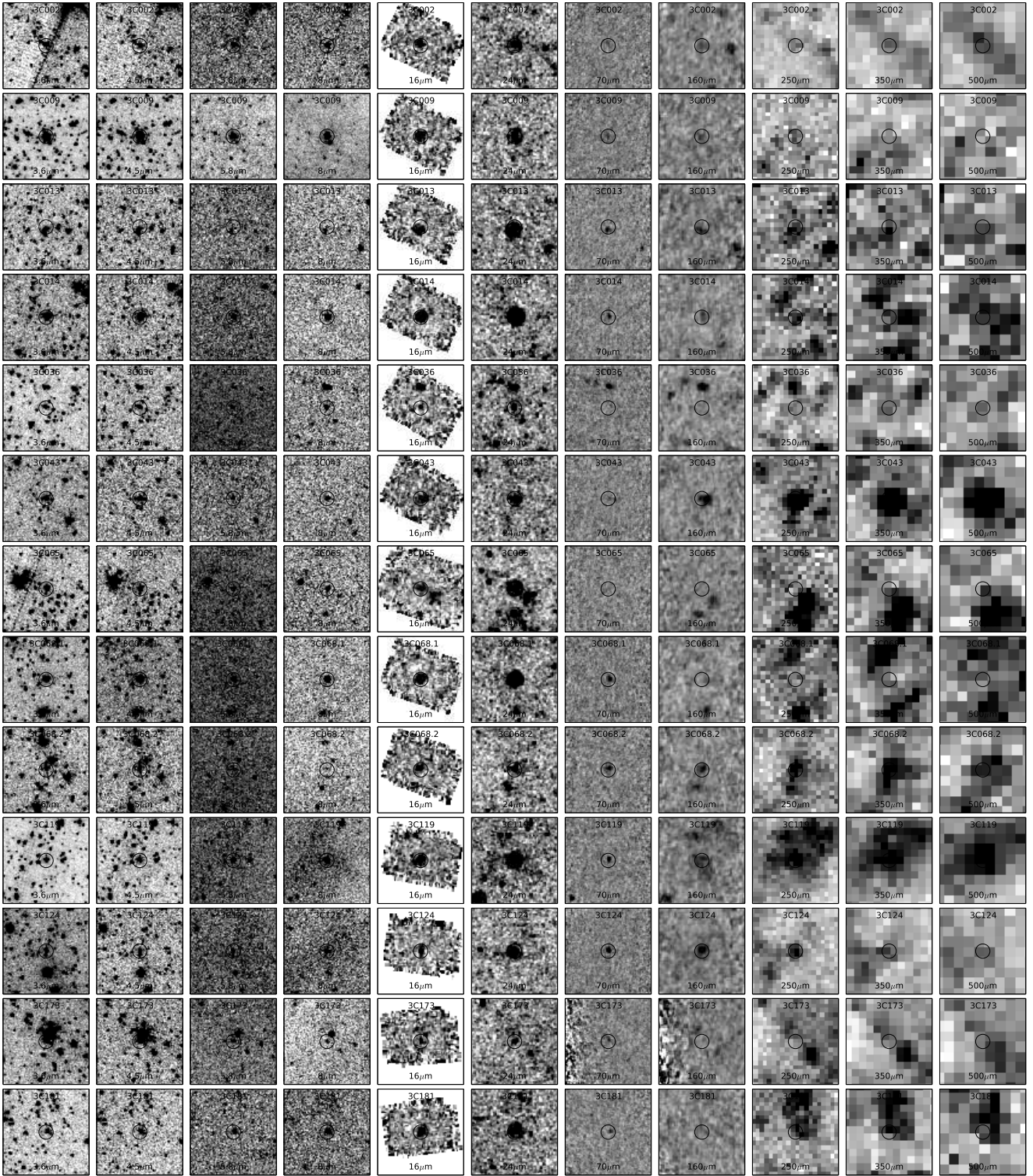


Fig. E.1. Postage stamps of the high- z 3CR objects studied in this work. From left to right: IRAC $3.6\ \mu\text{m}$, IRAC $4.5\ \mu\text{m}$, IRAC $5.8\ \mu\text{m}$, IRAC $8\ \mu\text{m}$, IRS $16\ \mu\text{m}$, MIPS $24\ \mu\text{m}$, PACS $70\ \mu\text{m}$, PACS $160\ \mu\text{m}$, SPIRE $250\ \mu\text{m}$, SPIRE $350\ \mu\text{m}$, and SPIRE $500\ \mu\text{m}$ bands, respectively. Each image shown here has dimensions of 2×2 arcmin. The circle ($10''$ in radius) indicates the central position of the source.

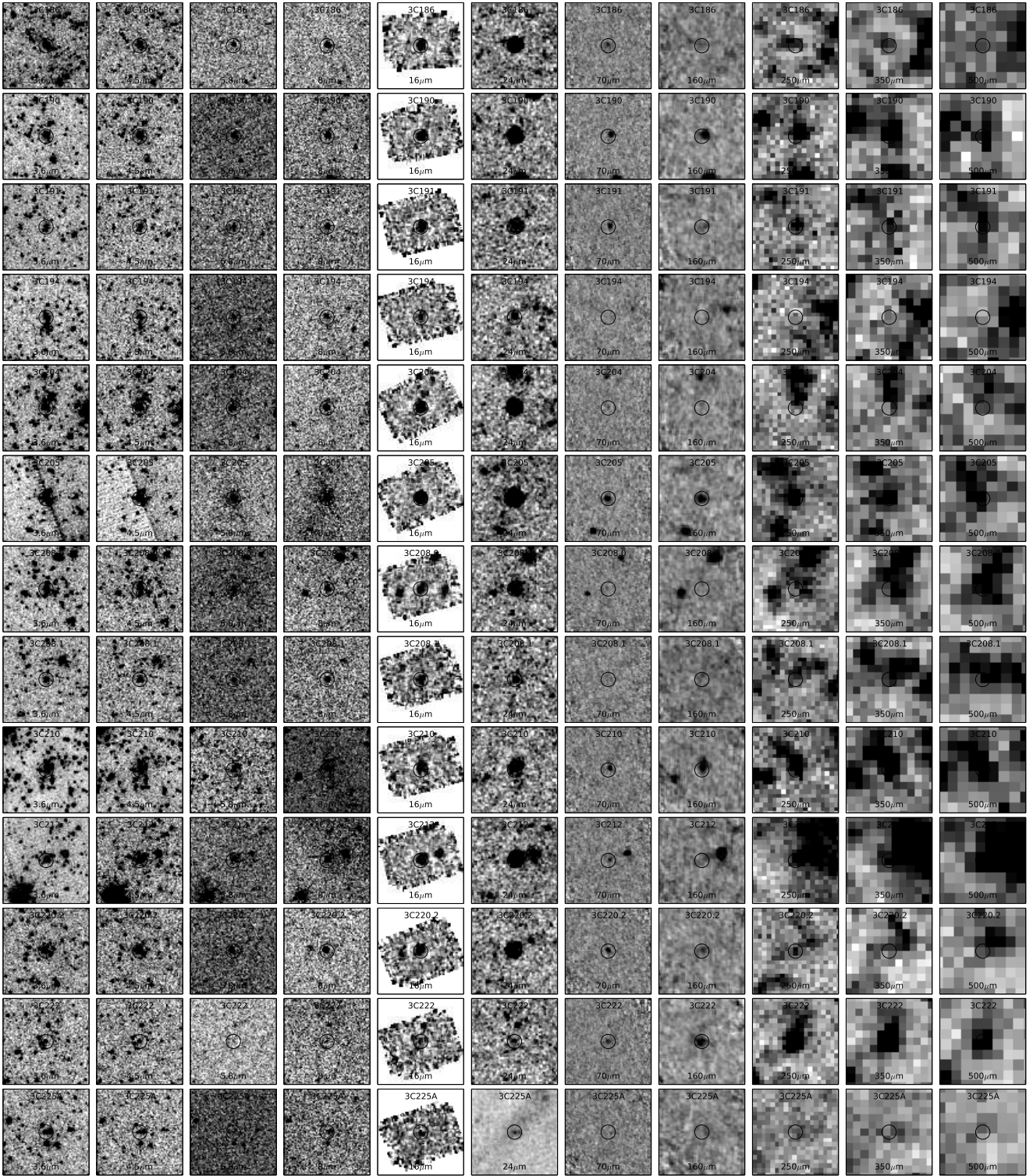


Fig. E.1. Continued.

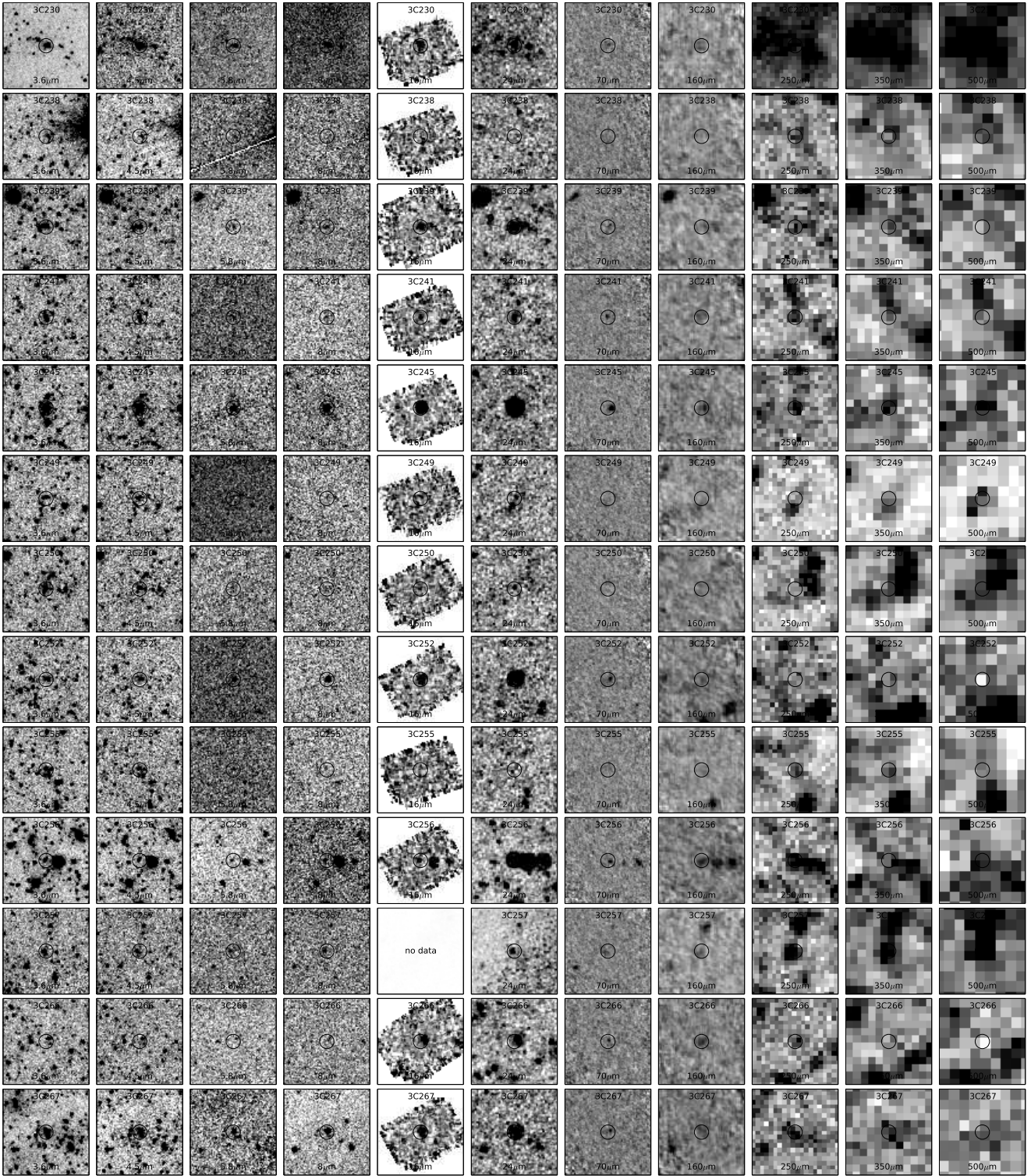


Fig. E.1. Continued.

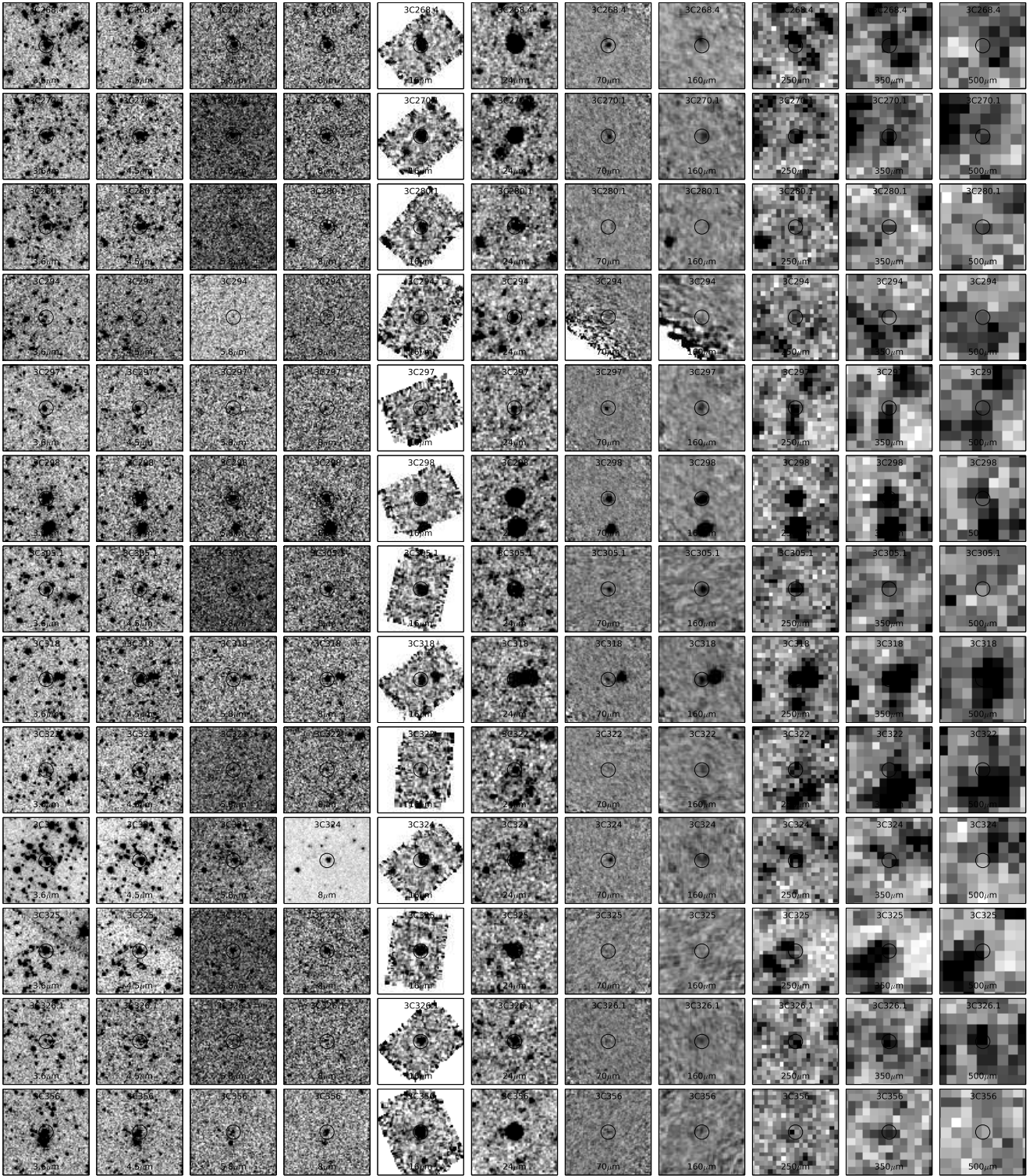


Fig. E.1. Continued.

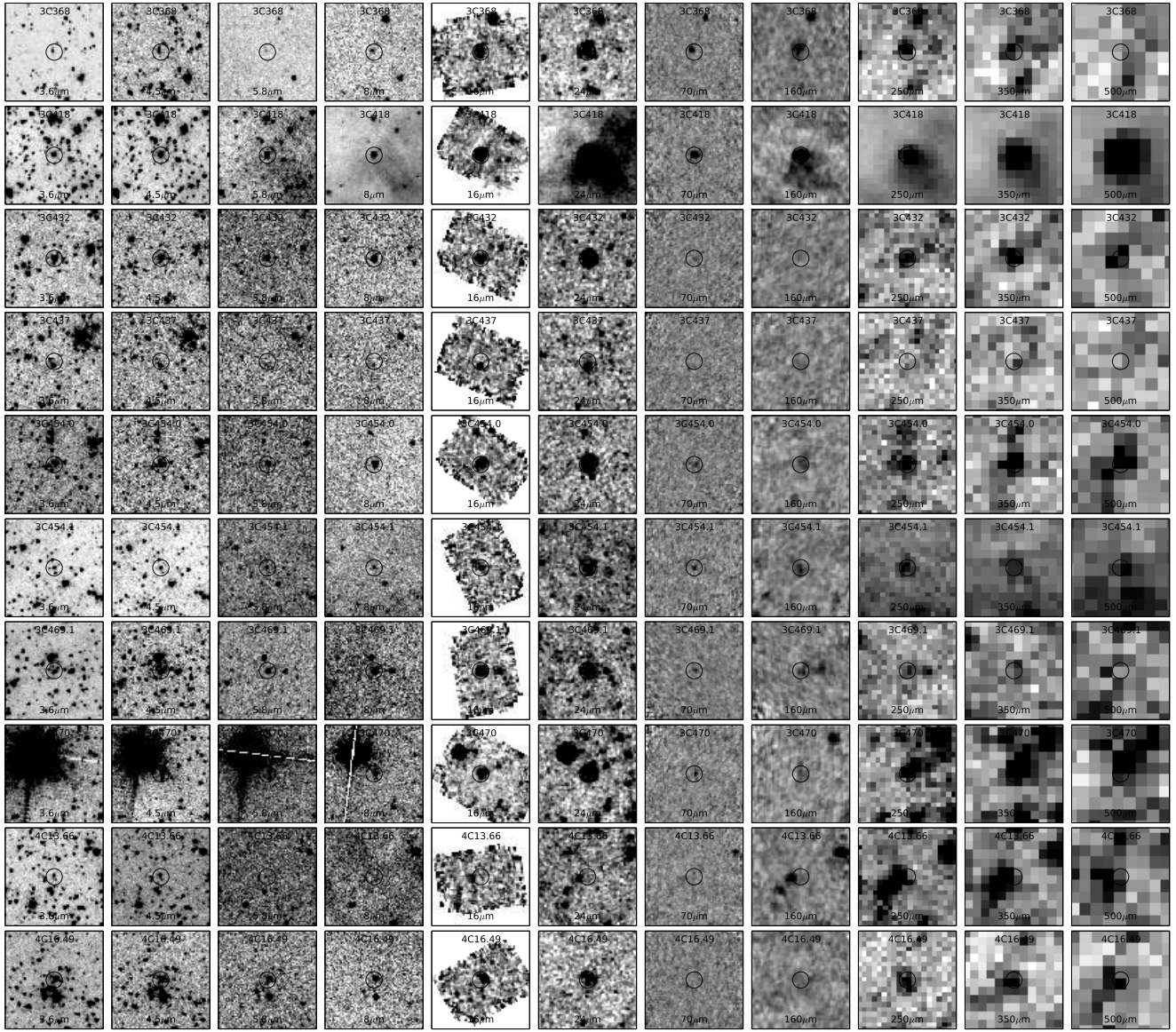


Fig. E.1. Continued.